ABSTRACT

PRABHUGOUD, MOHANRAJ Efficient Simulation of Bragg Grating Sensors for Implementation to Structural Health Monitoring of Composites. (Under the direction of Assistant Professor Kara Peters).

The goal of a structural health monitoring system is to detect, locate, and identify damages in a structure during its lifetime. The concept of structural health monitoring is particularly important for fiber reinforced composites due to the complexity of the possible failure mechanisms. The goal of this thesis is to simulate the response of optical fiber Bragg grating sensors to multi-component loading for their implementation in structural health monitoring algorithms for composites. A simulation method is presented to determine the effects of axial, bending and shear loading on an embedded optical fiber Bragg grating sensor. The effect of fiber bending on the Bragg grating sensor is experimentally verified by embedding the sensor in a solid cone, clamped at the base and subjected to a point load at the apex. Next, a numerically efficient method to calculate the response of sensors embedded in a unidirectional composite is developed using both finite element analysis and optimal shear-lag theory and taking into account the above effects. The limitations of the optimal shear-lag theory are derived through comparison with the finite element results. The application of this method is demonstrated through a numerical example, simulating the response of sensors embedded in one fiber layer to a transverse crack. This work is a first step towards the development of embedded sensors for fiber-reinforced composites that are "self evaluating".

Efficient Simulation of Bragg Grating Sensors for Implementation to Structural Health Monitoring of Composites

by

Mohanraj Prabhugoud

A dissertation submitted to the Graduate Faculty of
North Carolina State University
in partial satisfaction of the
requirements for the Degree of
Master of Science

Department of Mechanical and Aerospace Engineering

Raleigh

2002

Approved By:

Dr. F. G. Yuan

Dr. Kara Peters
Chair of Advisory Committee

Dr. Jeffrey W. Eischen

Biography

Mohanraj Prabhugoud was born in Bangalore, India on September 28, 1977. After completing his early schooling in Bangalore, he obtained a Bachelor of Engineering, B. E (Honors), degree from Bangalore University, India in 1999. He joined the Mechanical and Aerospace Engineering department at North Carolina State University in Spring 2001 to pursue his graduate studies.

Acknowledgements

The author would like to acknowledge the support of the North Carolina Space Grant Consortium who funded the data acquisition system used in the experiments. I would like to thank Dr. Kara Peters for advising and giving me the opportunity to work on this project. I would like to thank Dr. Michel Studer and Michael Camerino for their help in conducting the experiments, and Dr. Eric Klang and Dr. Chau Tran for allowing me to use the tensile testing machine. I would also like to thank Rufus (Skip) L. Richardson and Mike Breedlove for their help in machining the components required for conducting the experiments. I would like to thank Thomas R. Chapman of Corning Inc. for the optical fiber Bragg gratings.

Contents

List of Figures

List of Tables

Chapter 1

Introduction

The goal of a structural health monitoring (SHM) system is to detect, locate, and identify damages in a structure during its lifetime. From these evaluations, one determines appropriate mitigation actions to be taken, if applicable, and estimates the lifetime of the damaged structure. Ideally, such estimates should be made in semi-real-time during actual loading of the structure. Thus a successful SHM system would decrease catastrophic losses and become cost-effective as compared to regularly scheduled inspections [1]. The SHM must also be durable over the intended lifetime of the structure.

The concept of structural health monitoring is particularly important for fiber reinforced composites due to the complexity of the possible failure mechanisms [2]. The interactions of these various mechanisms makes lifetime predictions of composite structures extremely difficult and relatively uncertain. In addition, critical damage, assumed to be detected during scheduled inspections, is often non-visible on the surface of the laminated structure, necessitating embedded sensing systems. Due to the large range of failure mechanisms available for composite laminates, identifying the form of the damage, rather than strictly its size and location, is also crucial to make accurate lifetime decisions.

Due to significant improvements in ingress/egress packaging and signal processing, fiber optic sensors are rapidly becoming reliable and stable embedded measurement devices for fiber-reinforced composites [3]. Their greatest advantage is the ability to multiplex different types of strain sensors into a single, embedded measurement fiber, reducing the number of ingress and egress points required. However, as with any choice of embedded

sensor, fiber optic sensors are only useful for SHM systems if they can be integrated reliably into the host structure and the sensor measurements related to the physical changes of concern.

In this thesis, we consider the role of multi-component loading on an embedded sensor and the associated measurement issues. We present an analysis of embedded optical fiber sensors considering both the applied axial strain, shear strain and strain due to a local bending moment. The inclusion of multi-component loading in the calculation of the sensor response is important towards *(i)* locating and identifying the form of the damage, *(ii)* reducing errors in the damage identification process, and *(iii)* better recognizing the growth mechanisms of this damage.

In Chapter 2, we review different fiber optic sensors along with previous measurements of their response to non-axial loading. We also review a numerically efficient optimal shear-lag theory for obtaining stress distributions in a unidirectional fiber-reinforced composite. In Chapter 3, the response of the optical fiber Bragg grating sensor to axial loading, bending, and shear loading is simulated. In Chapter 4, the effects of these different components are experimentally verified. The dependence of bending loss on the radius of curvature of the optical fiber is also calculated. In Chapter 5, the response of the Bragg grating sensor embedded in one fiber layer of a fiber reinforced composite is simulated, as a transverse crack is propagated. The bending on the fiber is assumed to be significant only when the sensor is located near the damage, and the sensor response is calculated using a combined finite element/optimal shear-lag model. The results of these simulations and future work are discussed in Chapter 6.

Chapter 2

Background

2.1 Optical Fiber Sensors

The purpose of an optical fiber sensor is to encode a physical measurand (such as strain, acceleration, displacement, temperature, or pressure) into a change in physical properties of lightwaves propagating in the core of the fiber. These sensors can be categorized into measurements of the lightwave intensity, phase or spectrum. Some advantages of using fiber-optic sensors as compared to electrical strain gauges are that optical fibers:

- can be either surface mounted or embedded in composite materials
- are not susceptible to electromagnetic interference
- demonstrate excellent strain sensitivity

As an example of an intensity based fiber-optic sensor consider two optical fibers placed in close proximity to each other at their extremes [4]. Light is propagated through one of the optical fibers and when it exits expands into a cone of light whose numerical aperture depends on the difference between the index of refraction of the core and cladding of the optical fiber. The amount of light captured by the second optical fiber depends on its numerical aperture and the distance between the optical fibers. When this distance is modulated it in turn results in an intensity modulation of the light captured. Other examples of intensity based sensors are rotary and linear fiber-optic position sensors, and

sensors based on the principle of total internal reflection. The use of intensity based sensors is primarily limited due to variable losses in the system that are not related to the measurand such as fluctuations in the input laser power.

Interferometric based fiber-optic sensors have an extremely high sensitivity to strain due to their long active sensing length. One important application is in fiber-optic gyroscopes. Fiber-optic gyroscopes are being used to support automobile navigation systems, pointing and tracking of satellite antenna and inertial measurement systems for commuter aircraft [4]. Sagnac, Mach-Zehnder, and Michelson interferometers are the most widely used configurations for the phase measurement. The measurand acts on one arm of the fiber interferometer while the reference arm is isolated from the environment.

Spectrum based fiber-optic sensors depend on a lightwave being modulated in wavelength by an environmental effect. The Fiber Bragg grating (FBG) sensor is the most commonly used example of a spectral sensor. This sensor is fabricated by writing a grating, i.e. a modulation in the local refractive index, onto the core of an optical fiber as shown in Fig. 2.1. Bragg gratings are used for static strain monitoring, dynamic strain sensing, temperature measurements, and as filters in telecommunication systems.

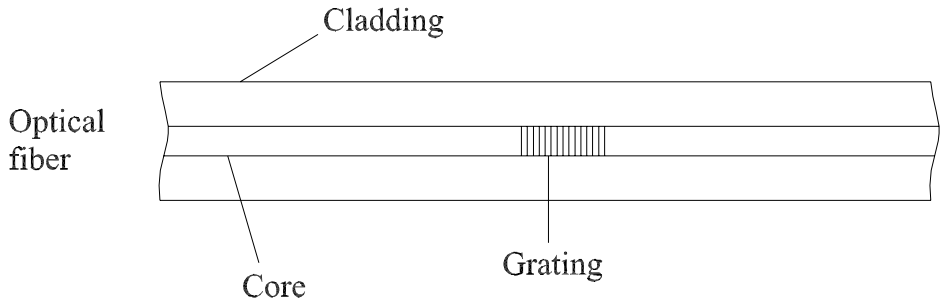

Figure 2.1: Bragg grating in the core of an optical fiber.

The principle of operation of a FBG sensor is that the maximum reflected wavelength of the grating changes due to strain or temperature as shown in Fig. 2.2. The

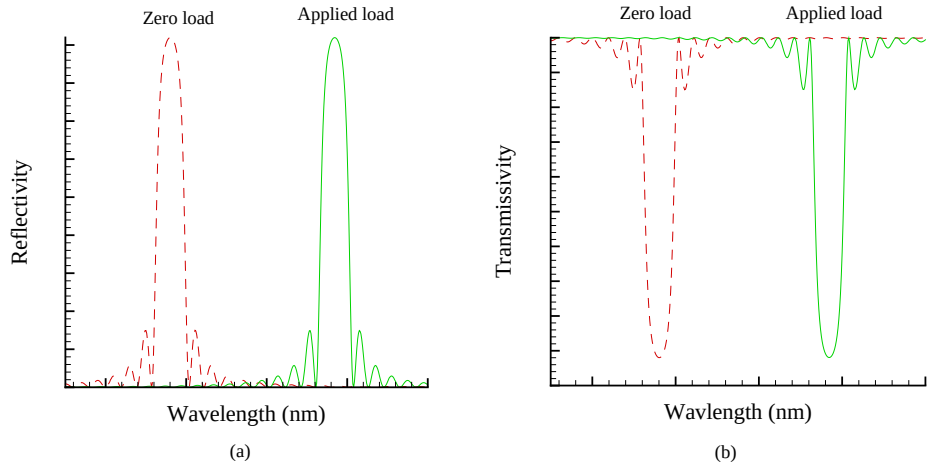

Figure 2.2: (a) Wavelength shift in reflected spectrum of a FBG due to applied load at constant temperature. (b) Wavelength shift in transmitted spectrum of a FBG due to applied load at constant temperature.

wavelength shift is linearly proportional to the applied strain or temperature. FBG sensors have been used in a number of applications such as structural health monitoring of carbon fiber reinforced polymer (CFRP) bridges and composite ship hulls, crack monitoring of concrete structures, CFRP composite cylinder pressure monitoring [3] and the determination of residual stresses in fiber-reinforced composite materials [8]. As compared to other optical fiber sensors, FBG's have particular, yet significant, advantages:

- Hundreds of FBG strain sensors can be multiplexed along a single fiber reducing the ingress/egress connections required[3];
- The FBG sensor yields absolute strain information.

Several different methods are currently used to write Bragg gratings in the core of an optical fiber [5]:

a. *The bulk interferometer*

A UV beam is divided into two beams at the beam splitter and then brought together at the mutual angle of θ, by reflections from two UV mirrors as shown in Fig.2.3. Interference fringes are formed at the fiber, mounted at the intersection of the beams. This method allows the Bragg wavelength to be chosen independently of the UV wavelength since the

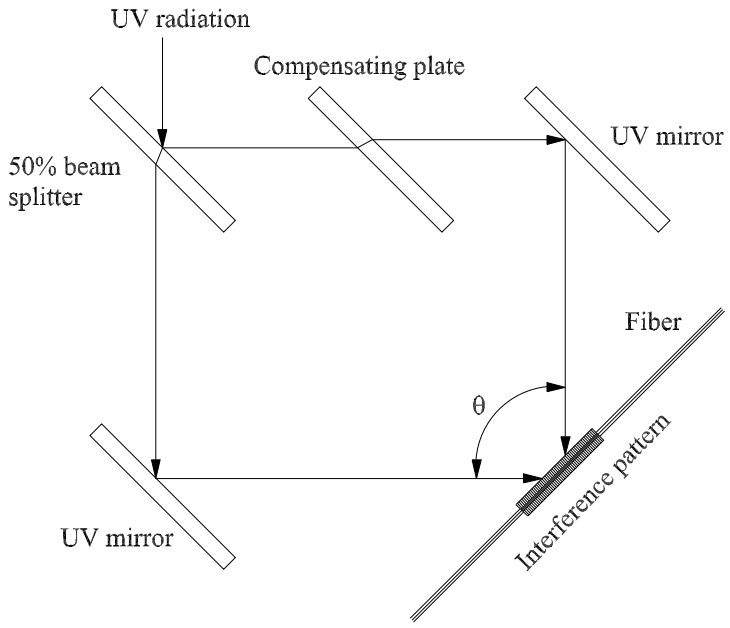

Figure 2.3: UV interferometer for writing Bragg gratings in optical fibers [5].

grating period formed depends upon θ. The disadvantage of this method is that it is highly sensitive to mechanical vibrations due to the long path lengths in air, thus limiting its application to short exposures.

b. *The phase mask interferometer*

Easier inscription of fiber gratings is possible by application of a phase mask to replace the interferometer. The phase mask is a relief grating etched in a silica plate. The depth of the etched sections of the grating is a function of the UV wavelength, but the period is dependent only on the Bragg wavelength and effective index of the mode. The phase mask acts as a diffraction grating, splitting the UV beam into m=0, ± 1 diffraction orders. The ± 1 orders are reflected by mirrors and combined to form a interference pattern in the fiber placed at the intersection of two orders as shown in Fig. 2.4. The zero order can be avoided in the region of the grating by repositioning the interferometer mirrors.

c. *Ultralong-fiber gratings*

To create longer FBG's a short interference pattern can be printed periodically in a continuously but slowly moving fiber. Using a pulsed laser, a short grating is imprinted in the fiber at any one time. The velocity of the fiber is sufficiently slow such that within the pulse

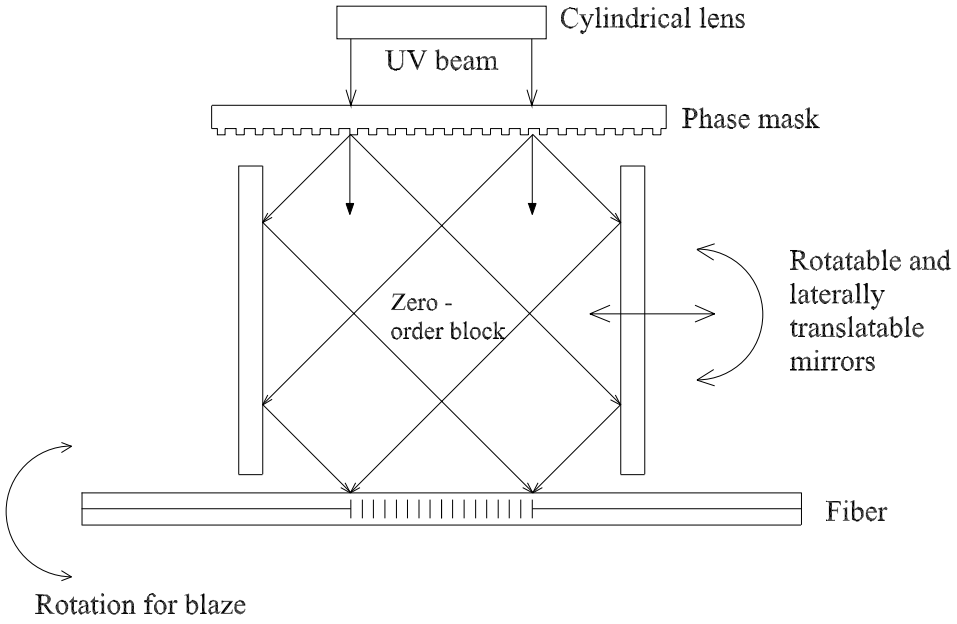

Figure 2.4: The phase mask used as a beam splitter in an interferometer for inscription of fiber gratings [5].

width, it may be regarded as being stationary. When the fiber has moved a few integral numbers of grating periods, a second pulse arrives, imprinting yet another grating partially overlapped with the previous grating but adding a few extra periods to the length.

Currently, FBG's are commercially available from a number of optical fiber manufacturers such as Corning, Fujikura Electric Company, Furukawa Electric Company, Hitachi Cable Company and Lucent Technologies.

Fig. 2.5 shows a typical setup to measure the reflected spectrum of a FBG. The laser illuminates the FBG through a coupler. The laser has a narrow output bandwidth and is wavelength tunable. The 3-way coupler (or circulator) transmits the light from the laser to the grating. The reflected light from the grating is transmitted to the photodetector through the same coupler. The optical signal is converted into a analog signal by the photodetector. This analog signal is then collected using a data acquisition system. For a range of wavelengths, the reflected intensity is measured forming the reflected spectrum of the FBG.

Due to their small size, optical fiber gages can be embedded unobtrusively into materials, particularly laminated composites already containing fiber reinforcements. Once an optical fiber is embedded, the interpretation of its gage response becomes more complex,

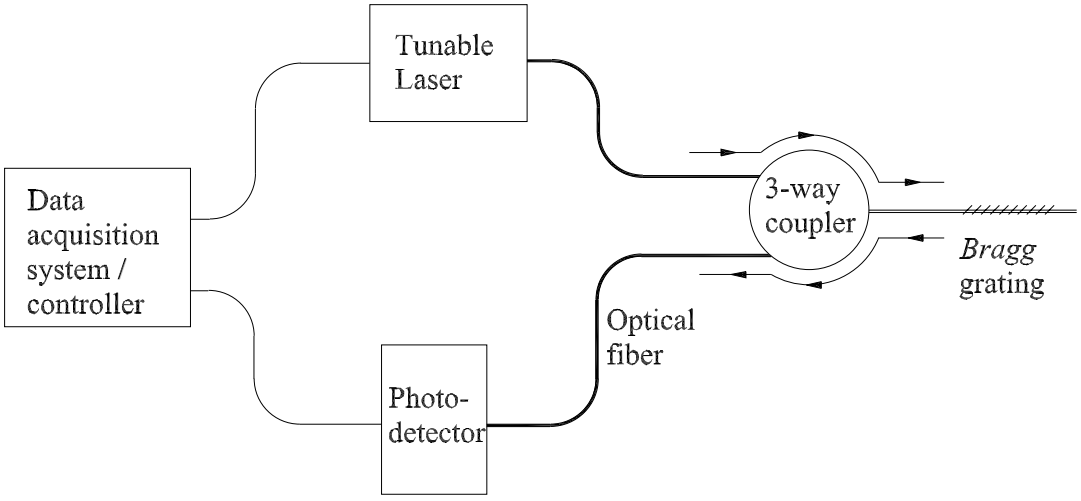

Figure 2.5: Typical instrumentation for FBG spectral analysis in reflection.

due to the effects of interface between the fiber and the material, as well as the multiple components of strain applied to the fiber. Analytical techniques exist for the calculation of stresses and strains in embedded fiber optic sensors due to applied far field stresses [6]. There can also be a degradation in the strength and material properties of the host material embedded with optical fibers. However, it has been shown by Measures[7] that embedded optical fibers with a diameter of less than 140 μm do not noticably reduce the ultimate strength or the fatigue life of typical graphite/epoxy specimens.

2.2 Response of optical fiber sensor to non-axial loading

The response of the FBG to axial strain (both constant and non-uniform) has been well characterized for strain sensing [11]. However, when the sensor is located near damage, other components of strain can affect the response of the FBG significantly, leading to erroneous strain interpretation.

Peters et al., embedded a FBG in an epoxy compact tension specimen as shown in Fig. 2.6 (a) [12]. The $10mm$ long grating was located perpendicular to the notch tip

such that the applied strain would be highly non-uniform. The axial strain applied to the grating was measured independently using electronic speckle pattern interferometry on the surface of the specimen.

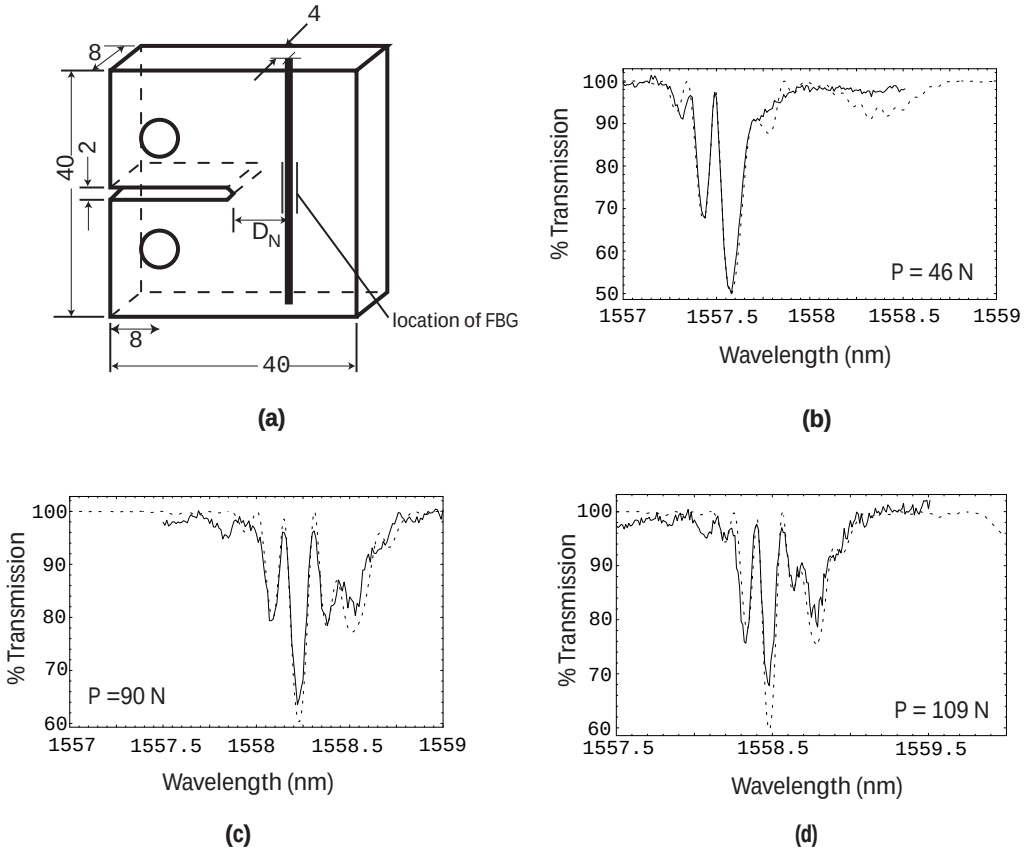

Figure 2.6: (a) Dimensions of the compact tension specimen with embedded optical fiber, (b),(c) and (d) grating response in tramission for 46, 90 and 109N applied load respectively [12].

Figures 2.6 (b), (c) and (d) show the spectral response of the grating in transmission for different magnitudes of applied load. Dashed lines represent the calculated gage response from the measured strain distribution. For lower loads the experimental and calculated spectra match well. Since the axial strain distribution is non-uniform, one observes multiple peaks in the transmitted spectrum (as will be explained in the following chapter). From the graphs, we also observe that there is a difference in the calculated and experimental gage response at higher applied loads. This difference appears only at higher loads and primarily in the peaks after the wavelength of maximum transmission. There was also no

permanent damage in the grating since the transmission spectrum at zero load before and after the loading was the same. Furthermore, there was no birefringence due to ellipticity of the cross-sectional area of the grating since the distance between the peaks was constant and not a function of wavelength. Therefore, the optical loss in transmitted intensity is due to effects other than the resulting axial strain on the grating, for example bending and shear losses.

To study bending losses of FBGs, Dai et al., subjected FBGs to pure bending tests [9]. They observed that the shift in Bragg wavelength is small and much smaller than that shift due to the extension strain for both normal and tilted gratings. They also observed that the reflected peaks were significantly deformed. The loss of transmission optical power due to macrobending was much larger than the increase in reflected optical power. The reason for this loss is that for reflection, only the backward propagating fundamental mode is measured by the powermeter, while for transmission under bending, the energy will be coupled into other modes, such as radiation modes, which are not measured.

Dong et al., mounted a chirped FBG on the lateral surface of a simply supported polymer beam [10]. During loading, they observed a proportional increase in the bandwidth of the FBG with the increase in curvature. They also observed that the wavelength shift is relatively small.

2.3 Optimal shear-lag theory for unidirectional composites

Shear-lag analysis is used as a tool for simplified stress analysis in composite materials. Due to a number of assumptions, the shear-lag method is computationally more efficient than the finite element method. It has been shown that shear-lag analysis, when used to analyse unidirectional composites, is more accurate for composites with high fiber/matrix stiffness ratios and for high fiber volume fractions [14]. Bending of fibers cannot be modeled using the 1-D shear-lag method because the shear-lag method is incapable of supporting the transverse shear that permits bending deformations. There are many other limitations to the types of problems that can be analyzed and to the type of results that can be generated by the shear-lag method [13]. In this work, the optimal shear-lag analysis developed by Nairn and Mendels, will be used. This theory models a 2D unidirectional lamina as a series of fiber and matrix layers. It includes the following assumptions:

- Linear shear stress distribution in each layer
- Shear behaviour is controlled only by the axial displacement of layers
- Layers are 1D spring elements, thereby neglecting the transverse stresses and the variations in the axial stress in the layer cross-sections

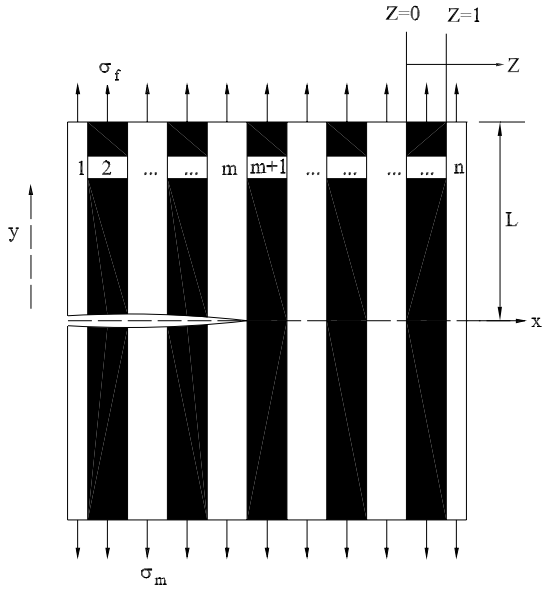

Figure 2.7: Model unidirectional composite for optimal shear-lag theory. This particular example has n fiber/matrix layers with an edge crack through the first m layers.

To derive the optimal shear-lag theory, as presented in [13], we consider the unidirectional model composite shown in Fig. 2.7. The composite consists of n fiber or matrix layers with an edge crack through the first m layers. The coordinate system is set such that $y = 0$ is at the crack. Both the fibers and matrix layers are considered isotropic with Young's moduli E_f and E_m respectively. z_i is the dimensionless coordinate in the x-direction in the i^{th} layer ranging between $z_i = 0$ at the left boundary and $z_i = 1$ at the right boundary. The composite is axially loaded at $y = \infty$ with fiber stress $\sigma_f = 1.0$ and matrix stress $\sigma_m = \frac{E_m}{E_f}$ to approximate a uniform remote force. Let u and v be displacements in the x and y directions respectively. The first shear-lag assumption yields a shear stress distribution in the i^{th} layer, $\tau_{xy}^{(i)}$, of the form

$$\tau_{xy}^{(i)}(x, y) = \tau(x_{i-1})L_i + \tau(x_i)R_i \tag{2.1}$$

where,

- $L_i(z_i) = 1 - z_i, R_i(z_i) = z_i$ are linear shape functions
- $\tau(x_i)$ is the interfacial shear stress at the interface between layer i and $i+1$ located at x_i (a function of y)

Using the second shear-lag assumption we find,

$$\tau_{xy}^{(i)} = G_{xy}^{(i)} \frac{\partial v}{\partial x} \Longrightarrow \frac{\partial v}{\partial z_i} = \frac{t_i}{G_{xy}^{(i)}} (\tau(x_{i-1}) L_i + \tau(x_i) R_i) \tag{2.2}$$

where t_i is the thickness of the i^{th} layer. Multiplying both sides of Eq.(2.2) by $(A - z_i)$, integrating by parts and appropriately selecting the value of A for layer i and $i+1$ gives the continuity equation

$$\begin{aligned} < v^{i+1} > - < v^i > = & \frac{t_{i+1} < (1 - z_{i+1}) R_{i+1} >}{G_{xy}^{(i+1)}} \tau(x_{i+1}) + \frac{t_i < z_i L_i >}{G_{xy}^{(i)}} \tau(x_{i-1}) \\ & + (\frac{t_{i+1} < (1 - z_{i+1}) L_{i+1} >}{G_{xy}^{(i+1)}} + \frac{t_i < z_i R_i >}{G_{xy}^{(i)}}) \tau(x_i) \end{aligned} \tag{2.3}$$

for $i = 1$ to $n - 1$. Here,

- $< . >$ is the average value over the layer
- $< v^i > = \frac{1}{t_i} \int_{x_{i-1}}^{x_i} v(x, y) dx = \int_0^1 v(z_i, y) dz_i$
- $G_{xy}^{(i)}$ is the shear modulus of layer i

Now we consider the stress equilibrium equation for the i^{th} layer

$$\frac{d}{dy}(t_i < \sigma_y^{(i)} >) = \tau(x_{i-1}) - \tau(x_i) \tag{2.4}$$

Using Hooke's law, the third shear-lag assumption and the continuity equation Eq.(2.3) we find

$$[A] \frac{d^2 \tau}{dy^2} - [B] \tau = 0 \tag{2.5}$$

where,

- $[A]$ and $[B]$ are tridiagonal matrices
- $\tau = (\tau(x_1), \tau(x_2), ..., \tau(x_{n-1}))$

Eq.(2.5) is a series of coupled second order differential equations with constant coefficients. They are solved by performing eigenvalue analysis, i.e. decoupling the system using the modal matrix and solving for each interface shear stress. Eq.(2.5) can also be transformed for determining the average axial stress in each layer. To do this, the differential equation Eq.(2.4) can be rewritten as,

$$\tau(x_i) = -\sum_{j=1}^{i} \frac{d(t_j < \sigma_y^{(j)} >)}{dy} \tag{2.6}$$

Substituting Eq.(2.6) into Eq.(2.5) we find,

$$\frac{d^2p}{dy^2} - [M_\sigma]p = \frac{E^{(i)}}{E_f} \tag{2.7}$$

where,

- $p = (t_1 < \sigma_y^{(1)} >, t_2 < \sigma_y^{(2)} >, ..., t_{n-1} < \sigma_y^{(n-1)} >)$
- $E^{(i)}$ is the modulus of elasticity of the i^{th} layer
- $[M_\sigma] = [I_L]^{-1}[A]^{-1}[B][I_L]$, $[I_L]$ is the unit lower triangular matrix

Solving the above systems, Eq.(2.7) yields,

$$< \sigma_y^{(i)} >= \frac{E^{(i)}}{E_f} + \sum_{j=1}^{n-1}(a_j e^{\lambda_j y} + b_j e^{-\lambda_j y})\frac{\psi_{j,i}}{t_i} \tag{2.8}$$

$$\tau(x_i) = \sum_{j=1}^{n-1}(a_j e^{\lambda_j y} - b_j e^{-\lambda_j y})\omega_{j,i} \tag{2.9}$$

where,

- λ_j is the jth eigenvalue of $[M_\sigma]$ and $[A]^{-1}[B]$ (eigenvalues of both matrices are the same)
- a_j, b_j are constants to be calculated from the boundary conditions
- $\psi_{j,i}$ is the i^{th} element of the j^{th} eigenvector of $[M_\sigma]$
- $\omega_{j,i}$ is the i^{th} element of the j^{th} eigenvector of $[A]^{-1}[B]$

For the unidirectional composite shown in Fig. 2.7, the following boundary conditions would be applied to calculate the $2n$ unknown constants a_j and b_j:

- As $y \to L$ the stress in each layer approaches the remote stress, i.e.

$$< \sigma_y^{(i)} >= \frac{E^{(i)}}{E_f} \Longrightarrow \sum_{j=1}^{n-1} (a_j e^{\lambda_j L} + b_j e^{-\lambda_j L}) \frac{\psi_{j,i}}{t_i} = 0$$

- The crack surface is a free surface, i.e. $< \sigma_y^{(i)} >= 0$ at $y = 0$ for layers 1 through m

$$\sum_{j=1}^{n-1} (a_j + b_j) \frac{\psi_{j,i}}{t_i} = \begin{cases} -\frac{E_m}{E_f}, & \text{i odd} \\ -1, & \text{i even} \end{cases}$$

- Setting $< v^{(11)} >= 0$ at $y = 0$ and using continuity equation for

$$< v^{(10)} >= 0, < v^{(9)} >= 0, ... < v^{(6)} >= 0$$

Nairn and Mendel [13] demonstrated that the optimal shear-lag theory compared closely with finite element results for a one-quarter model of a center crack specimen. The accuracy of the shear-lag results was best for composites with a high E_f to E_m ratio.

Chapter 3

Sensor Simulation

3.1 Simulation of FBG sensor response

The optical fiber Bragg grating is a periodic modulation in the index of refraction along a given length of the optical core, fabricated by UV irradiation of the fiber. Due to coupling between forward and backward propagating modes, some wavelengths of light are reflected rather than transmitted by the fiber at the location of the grating. The reflected spectral response for such a grating is shown in Fig. 2.2. The wavelength at which maximum reflection occurs, λ_B, is called the Bragg wavelength and is given by [11]

$$\lambda_B = 2n_{eff}\Lambda \tag{3.1}$$

where n_{eff} is the effective mode index of the optical fiber and Λ is the period of the grating.

To describe the Bragg grating, the modulation in effective index of refraction along the fiber axis, δn_{eff}, can be written as [15]

$$\delta n_{eff}(z) = \overline{\delta n}_{eff}(z)\{1 + \nu \cos[\frac{2\pi}{\Lambda}z + \phi(z)]\} \tag{3.2}$$

where z is the variable along the axis, $\overline{\delta n}_{eff}$ is the "dc"index change spatially averaged over a grating period, and ν is the fringe visibility of the index change. The function $\phi(z)$ describes the grating chirp and will be used later to introduce axial effects such as applied strain. A grating chirp can also be introduced through a non-constant amplitude

$\overline{\delta n}_{eff}(z)$. Fig. 3.1 shows the variation of $\delta n_{eff}(z)$ for different types of non-uniformities. Non-uniform gratings (or "chirped") are used for several purposes. For example, the raised-cosine-apodized chirping, shown in Fig. 3.1 (c), reduces the undesirable sidelobes prevalent in uniform grating spectra.

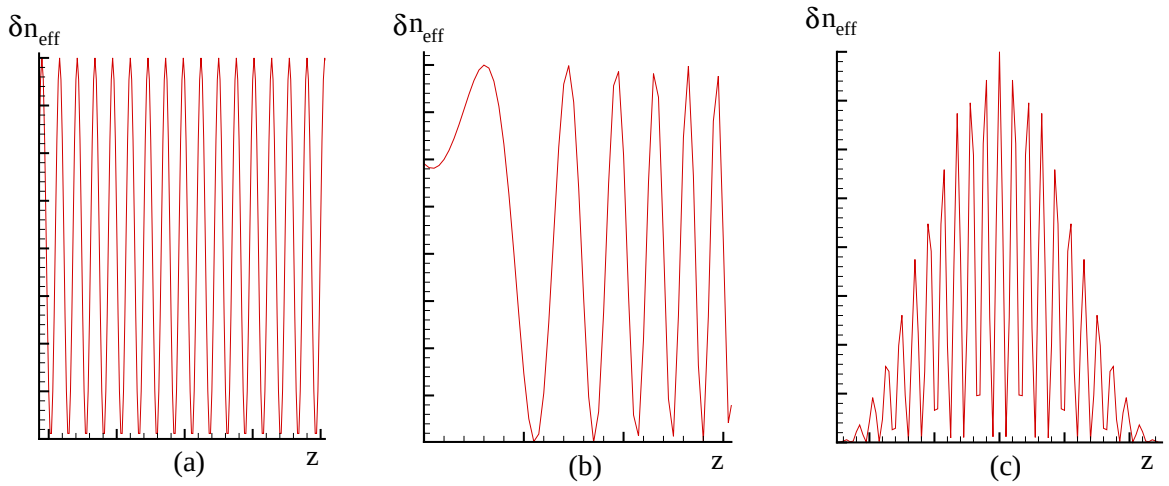

Figure 3.1: (a) Index of refraction variation of uniform optical fiber Bragg grating (size of grating period with respect to length of grating is exaggerated to show features); (b) index of refraction variation of "chirped"grating (i.e. $\phi(z) \neq 0$); (c) index of refraction variation of raised-cosine-apodized grating.

In order to calculate the reflectivity of an optical fiber Bragg grating as a function of the propagated wavelength, one solves the coupled first order differential equations defining mode propagation through the Bragg grating for a given wavelength [15],

$$\begin{aligned} \frac{dR(z)}{dz} &= i\hat{\sigma}R(z) + i\kappa S(z) \\ \frac{dS(z)}{dz} &= -i\hat{\sigma}S(z) - i\kappa R(z) \end{aligned} \tag{3.3}$$

In Eq.(3.3), $R(z)$ and $S(z)$ are the amplitudes of the forward and backward propagating modes as shown in Fig. 3.2. $\hat{\sigma}$ is the general "dc"self-coupling coefficient defined by

$$\hat{\sigma} = 2\pi n_{eff}(\frac{1}{\lambda} - \frac{1}{\lambda_D}) + \frac{2\pi}{\lambda}\overline{\delta n}_{eff} - \frac{1}{2}\frac{d\phi}{dz} \tag{3.4}$$

where λ_D is the design wavelength. κ is the "AC"coupling coefficient defined by

$$\kappa = \frac{\pi}{\lambda}\nu\overline{\delta n}_{eff} \tag{3.5}$$

The above coupled differential equations are solved using the following boundary conditions: $R(-L/2) = 1$ and $S(L/2) = 0$, which corresponds to a constant input spectrum at $z = -L/2$. Once solved, the reflection spectrum is calculated from the amplitude and power reflection coefficients $\rho = S(-L/2)/R(-L/2)$ and $r = \mid \rho \mid^2$, respectively. The transmission spectrum can then easily be found as $r_{transmission}(\lambda) = 1 - r_{reflection}(\lambda)$.

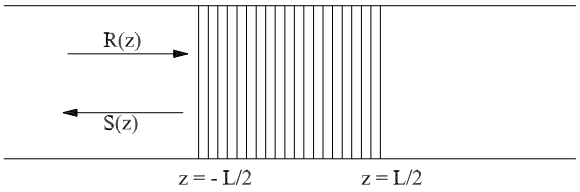

Figure 3.2: Geometry defining z coordinate of the Bragg grating and forward and backward propagating modes.

If the grating is uniform along z, then $\overline{\delta n}_{eff}$ is a constant, $d\phi/dz = 0$, and thus κ and $\hat{\sigma}$ are constants. Eq.(3.3) reduces to first order ordinary differential equations with constant coefficients for which a closed form solution exists [15]. The Bragg wavelength is then related to the design wavelength by,

$$\lambda_B = (1 + \frac{\overline{\delta n}_{eff}}{n_{eff}})\lambda_D$$

For a non-uniform grating the differential equations must be solved numerically. The fourth order Runge-Kutta method with variable step size is used in this work because of the following advantages [18]:

- the global error is $O(h^4)$; where h is the step size
- the Runge-Kutta method is a numerically stable algorithm

First, the boundary conditions are transformed to equivalent conditions at $z = \frac{L}{2}$ and integration is performed backward from $z = \frac{L}{2}$ to $z = -\frac{L}{2}$ to obtain $R(-\frac{L}{2})$ and $S(-\frac{L}{2})$. The step size in each integration step is controlled by the maximum allowable error. This is shown schematically in Fig. 3.3. For each step, R_{temp} and S_{temp} are computed for a single step of size h, and R_2 and S_2 are computed via two steps each of size $\frac{h}{2}$. If the absolute

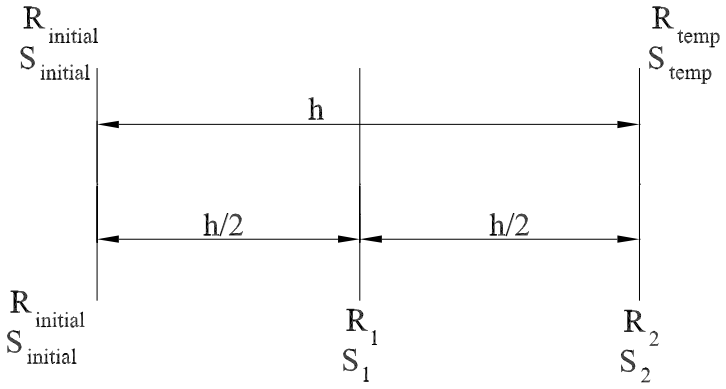

Figure 3.3: Parameters that control the step size for Runge-Kutta simulation of FBG spectra.

difference between R_{temp} and R_2 and between S_{temp} and S_2 is less than the allowable error in each step then $R_{initial} = R_{temp}$ and $S_{initial} = S_{temp}$ for the next step. Otherwise, the step size is reduced by half and the above procedure is repeated untill the error is less than the allowed value. Although time-consuming, this method produces results with a well controlled maximum error.

When the Bragg grating is used as a strain sensor, the applied axial strain, $\epsilon_z(z)$, changes the grating period according to,

$$\Lambda(z) = \Lambda_0(1 + \epsilon_z(z)) \tag{3.6}$$

where, Λ_0 is the initial grating period at zero strain. The axial strain can be introduced into the grating chirp function of Eq.(3.2) by [11]

$$\phi(z) = -\frac{2\pi}{\Lambda_0}\frac{\epsilon_z(z)}{1 + \epsilon_z(z)}z$$

Fig. 3.4 shows the simulated response of a uniform Bragg grating for three different cases of applied strain. We observe the following points:

- For the case of constant strain there is a shift in the Bragg wavelength but no change in bandwidth;
- For the case of linear strain there is an increase in bandwidth but no global shift;
- For the cases of constant and linear strain the reflectivity plot remains symmetric about the Bragg wavelength;

- For the case of quadratic strain symmetry of the spectrum is not maintained and there is a global shift of the spectrum to higher wavelengths.

3.2 Reflectivity loss due to bending moment

When bending is applied to the grating there is a loss in reflectivity due to the curvature of the optical fiber, referred to as the bending loss. From Fig. 2.6 we observed that although the grating was subjected to an axial load, small amounts of other components such as bending or shear were also acting on the grating at higher loads. These components give rise to a decrease in reflected intensity at the Bragg wavelength which cannot be explained by an equivalent axial strain. This bending loss is wavelength and spatially dependent (i.e. a function of λ and z). For an optical fiber without a Bragg grating, Taylor derived the power loss, ΔP, for a section of circular bend of radius r and length h, to be [16],

$$\Delta P(\lambda, h) = [(\overline{\kappa})(h)]^2 \tag{3.7}$$

where $\overline{\kappa(r)}$ is the "geometrical"coupling coefficient between the fundamental propagating mode and other guided and radiation modes. The effects of induced birefrigence on propagation are neglected. For the Bragg grating we introduce,

$$\Delta P = (\kappa f(1/r)h)^2$$

where, κ is the "AC"coupling coefficient given in Eq.(3.5), h is the segment length of the grating (to be used as the Runge-Kutta step-size), and $f(1/r)$ is a function of curvature that increases with applied curvature. To demonstrate this bending loss function consider the grating whose properties are given in Fig. 3.4 subjected to an quadratic axial strain and bending such that $f(1/r)h\ \alpha\ 1/(1+\epsilon)$. The exact form of the function $f(1/r)$ will be determined experimentally in the following chapter. For each wavelength, the above bending loss calculated for each step size h is added together. This total optical loss is subtracted from reflectivity for that particular wavelength. The step size for the given error is controlled by the applied strain. For all simulations, we assume small displacements and thus small strains. An example spectrum using this bending loss formulation is shown in Fig, 3.5. One observes that the fiber bending results in decreased reflectivity, particularly at wavelengths reflected at regions of higher bending. These are the same effects observed in Fig. 2.6.

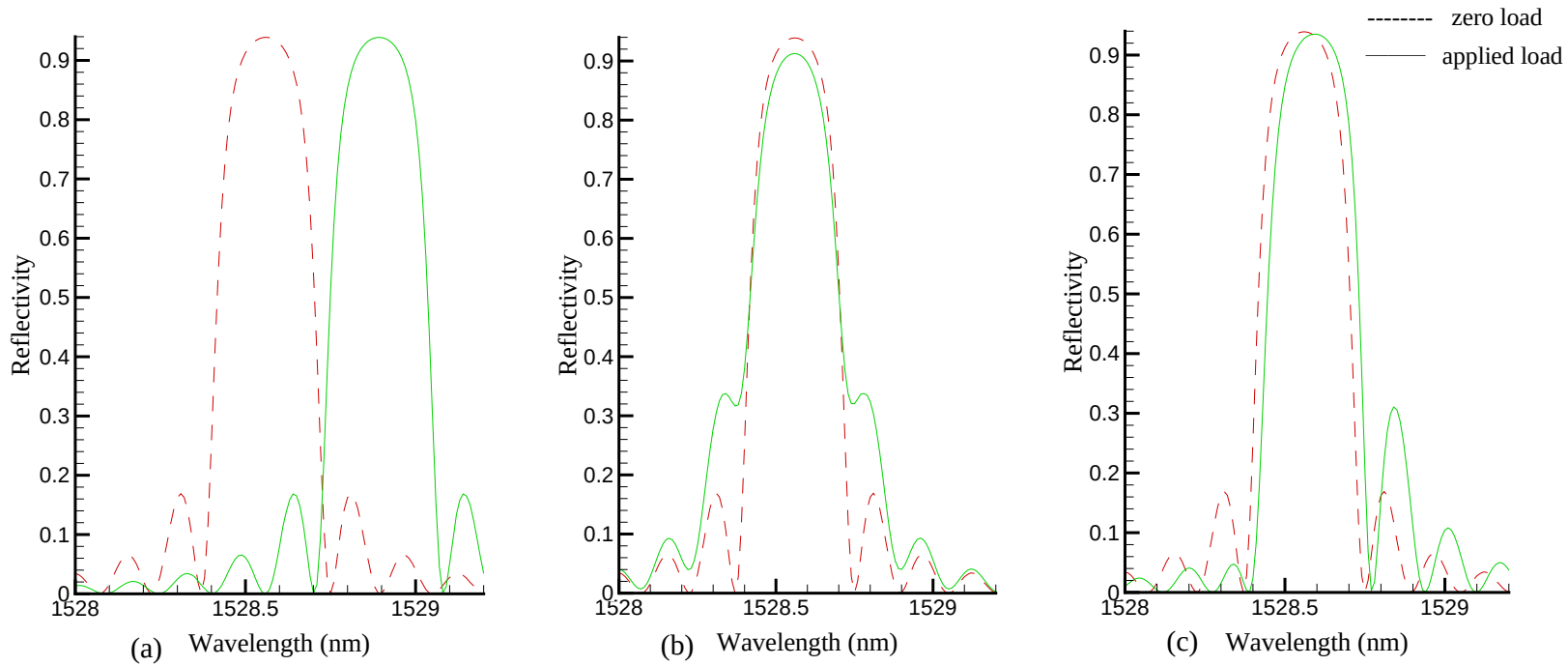

Figure 3.4: Reflectivity of Bragg grating for three different cases of applied strain. The following grating properties were assumed: $L = 5mm, \lambda_D = 1528.5nm, \overline{\delta n}_{eff} = 2\times10^{-04}, n_{eff} = 1.46$. Axial strain applied: (a) $\epsilon_z = 200\times10^{-06}$, (b) $\epsilon_z = (2\times10^{-11}/mm)z$, (c) $\epsilon_z = (5\times10^{-18}/mm^2)z^2$.

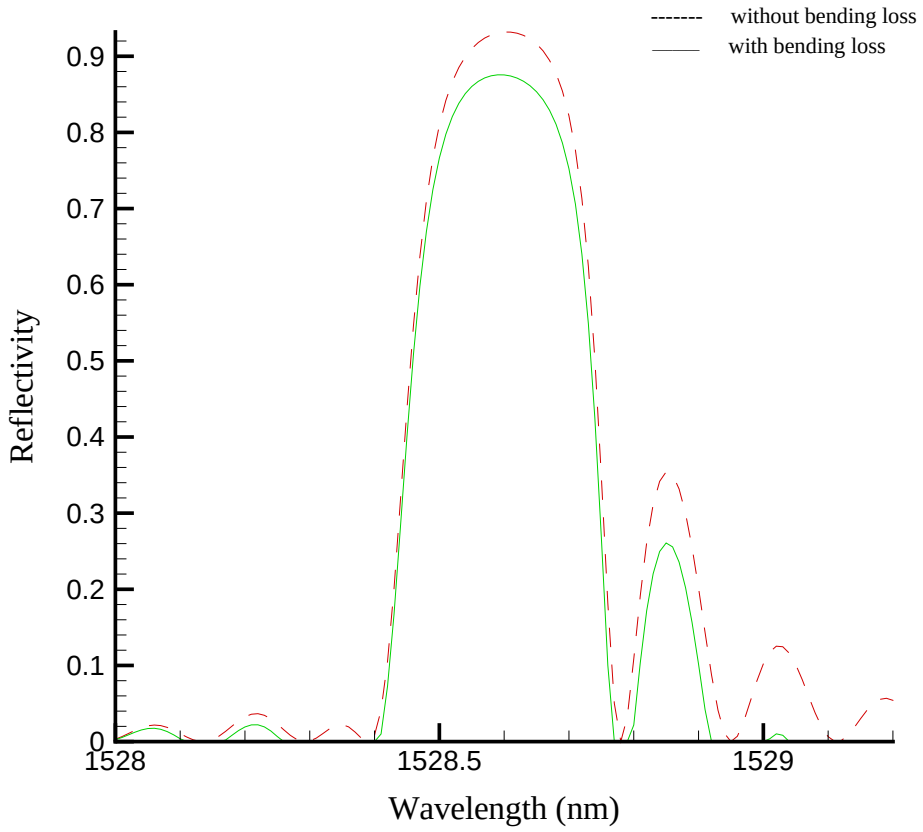

Figure 3.5: Reflectivity of Bragg grating calculated with and without loss function due to fiber bending. Resulting axial strain due to applied bending moment $\epsilon_z = (10 \times 10^{-18}/mm^2)z^2$. Properties of grating are given in Fig. 3.4.

3.3 Reflectivity loss due to shear loading

In contrast to the bending moment case discussed above, the primary effect of shear loading on a Bragg grating is apparent through the change in fringe visibility, ν, of the grating (see Eq.(3.2)). As shown in Fig. 3.6, the applied shear loading τ results in an angle θ, equivalent to the shear strain γ, between the axis of the grating and the longitudinal axis of the fiber. The change in period of the grating due to the applied shear stress is negligible compared to the change in fringe visibility. For small deformations, the modified fringe visibility function ν, is given by [15],

$$\nu = cos(\theta) \tag{3.8}$$

Figure 3.7 plots the reflected spectrum of a typical Bragg grating with and without applied shear loading. The region of the plot is magnified to that near the Bragg wavelength in order to distinguish between the two curves. Note that the applied shear strain for the case plotted is extremely large. Thus the magnitude of shear strain must be relatively high to obtain a significant change in the reflection coefficient of the grating. Therefore, the applied shear will be neglected in the later embedded fiber simulations. The presence of a coating on the optical fiber would also significantly diminish the shear transfer to the optical fiber, further reducing this effect [17].

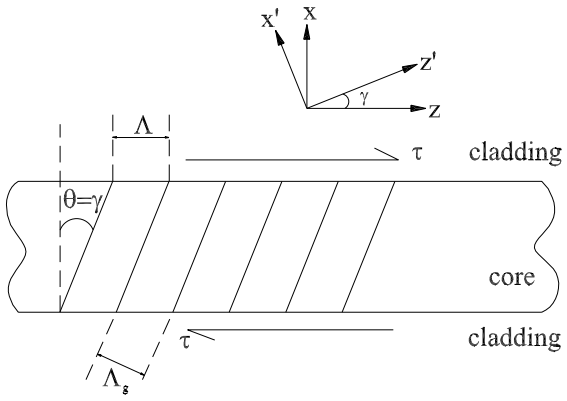

Figure 3.6: Definition of θ for fringe visibility function $\nu(\theta)$.

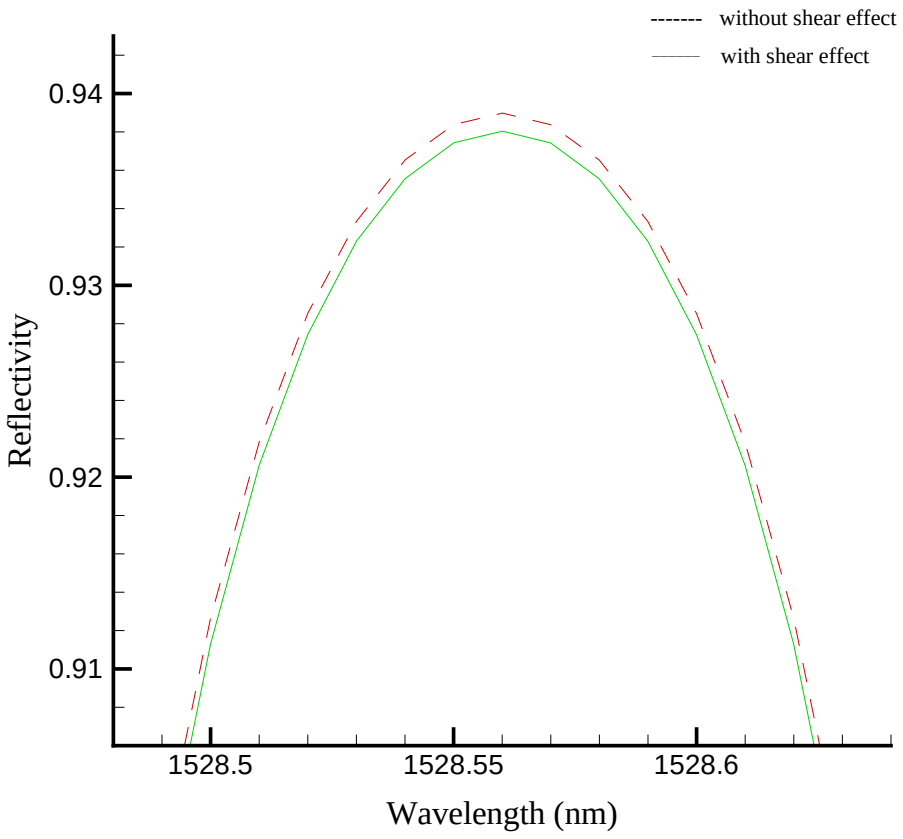

Figure 3.7: Change in reflection due to an applied pure shear of $\gamma = 0.08727$ for the FBG whose properties are given for Fig. 3.4.

Chapter 4

Experimental determination of sensor response to bending

The goal of this chapter is to measure the Bragg grating reflectivity loss due to fiber bending and its dependence on the radius of curvature for comparison with the sensor response model of Chapter 3. In order to experimentally determine this dependence, we embed a Bragg grating in a conical, isotropic specimen. The specimen is cantilevered at the base and subjected to a point load at the apex. As the exact strain field solution is known, we simulate the response of the grating to a non-uniform axial strain along its axis and compare it with the experimental response. The difference in the simulated and experimental response is the bending loss. Section 4.1 presents the exact strain solution for the specimen due to the applied loading. Sections 4.2 and 4.3 explain the procedure for preparing the specimen from epoxy resins and the design of the loading frame. The final section presents the experimental results and the calculation of the bending loss function.

4.1 Exact solution for an isotropic cone subjected to bending moment and shear

In order to find the dependence of the bending loss on the radius of curvature, we consider a solid cone geometry, cantilevered at one end and subjected to a shear force at the other end. The cone geometry is considered because the exact solution (displacement field) for several different types of loading is given by Renton [19, 20]. The cone geometry possesses two axes of symmetry. Spherical coordinates are used, defining r as the length of the radius vector from the origin (apex of the cone), θ as the angle of the radius vector to the axis of the cone and ϕ as the clockwise angle of the radius vector from the datum. These coordinates are shown in Fig. 4.1. The displacements in the direction of increasing r, θ, and ϕ are u, v, and w respectively. The displacement field and the radial strain for a solid cone subjected to a pure bending moment M are given by [19],

$$\begin{aligned} u &= \frac{1}{Gr^2}[2At + C(5-4\nu)sin\theta cos\theta]sin\phi \\ v &= \frac{1}{Gr^2}[-A(1+t^2) + B + C((4\nu-2)sin^2\theta - 1)]sin\phi \\ w &= \frac{1}{Gr^2}[-A(1+t^2) + Bcos\theta - Ccos\theta]cos\phi \\ \epsilon_{rr} &= \frac{-4sin\theta(1+\nu)sin\phi}{Er^3(1+cos\theta)}[2A + C(5-4\nu)cos\theta(1+cos\theta)] \end{aligned} \tag{4.1}$$

where, $t = tan(\theta/2)$, and G is the shear modulus. The constants A, B, and C are calculated by applying free surface boundary conditions at $\theta = \alpha$ (i.e. $\sigma_{\theta\theta} = \tau_{r\theta} = \tau_{\theta\phi} = 0$) and the applied bending moment, M, about $\phi = 0$. We note from Eq.(4.1) that the displacements are proportional to $1/r^2$, thus the stresses are proportional to $1/r^3$. To calculate the displacement field for a solid cone subjected to pure shear, we consider the solution of a hollow cone subjected to pure shear [20] and by appropriately selecting the constants derive the solution for the solid cone. The displacement field and the radial strain obtained after the selection of constants are given by,

$$\begin{aligned} u &= \frac{1}{Gr}[4A(1-\nu)sin\theta + Ctan\theta]cos\phi \\ v &= \frac{1}{Gr}[A(3-4\nu)cos\theta + B(1+t^2) + C]cos\phi \\ w &= \frac{1}{Gr}[-A(3-4\nu) - B(1+t^2) - C]sin\phi \end{aligned}$$

$$\epsilon_{rr} = \frac{-2sin\theta cos\phi}{Er^2(1+cos\theta)}[4A(1+cos\theta)(1-\nu^2)+C(1+\nu)] \tag{4.2}$$

One notes from Eq.(4.2) that the stresses are proportional to $1/r^2$. The constants A, B, and C are calculated by applying the free surface boundary conditions and the tip shear force S acting in the positive θ direction in the plane $\phi = 0$.

In the following experiment an optical fiber was embedded in the cone along the line $\theta = \theta_1$, $\phi = \phi_1$ as shown in Fig. 4.1. For each of the above loading cases, the axial strain in the fiber is given by ϵ_{rr}, and the local curvature of the fiber can be calculated as $\kappa_r = \partial^2 v/\partial r^2$.

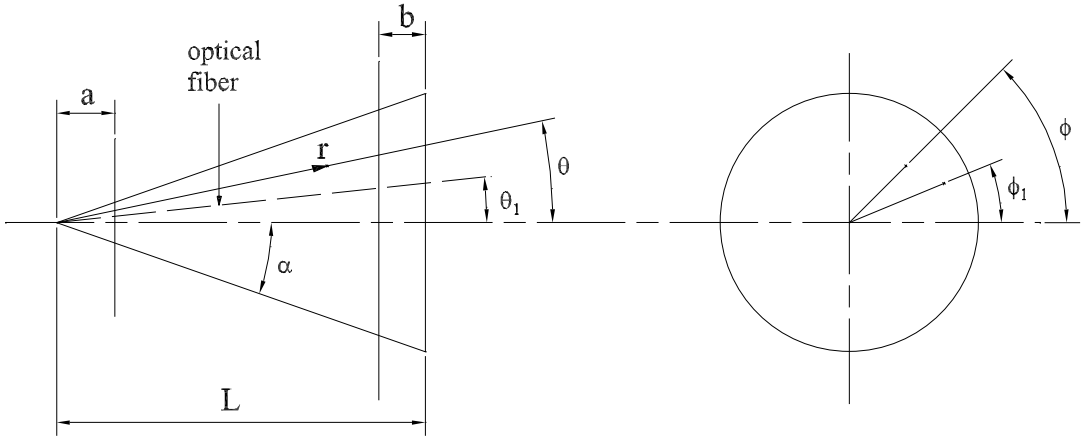

Figure 4.1: Geometry of the cone defining spherical coordinates r, θ, and ϕ. a defines the distance from apex to the loading point, b defines the distance from the base to the clamping point, and θ_1, ϕ_1 are the corresponding angles of orientation of the optical fiber with respect to the axes of the cone.

Resin	Weight Fraction	Total weight
D.E.R 330	w	37.5 g
D.E.R 732	$w \cdot 15/35$	16.07 g
D.E.H 24	$w \cdot 10/35$	10.71 g

Table 4.1: Composition of epoxy specimen.

4.2 Specimen preparation

In order to embed the sensor in the epoxy resin, the conical specimen was molded in the laboratory. The machine drawings for the mold are given in Appendix A. The composition of Dow Chemical epoxy resins used are D.E.R 330 (polymer of epichlorohydrin and bisphenol A), D.E.R 732 (polymer of epichlorohydrin and polyglycol), and D.E.H 24 (Triethylenetetramine). The proportions of the two epoxy resins and the curing agent used are given in Table. 4.1. The specimen length was sufficient such that the grating is neither close to the apex nor the base of the cone. Since the solidification process of epoxy is an exothermic reaction, the volume of epoxy poured into the mold was limited to prevent internal boiling. Hence, the specimen was prepared in layers with each layer having same composition and volume of epoxy.

Before pouring the first layer, the mold was prepared by applying one coat of carwax and two coats of mold releaser. The fiber was placed in the mold so that it is neither close to the surface nor to the center axis. The two epoxy resins namely D.E.R 330, and 732 were mixed in the proportions given in Table. 4.1 and heated to approximately $60°C$ for 5 minutes so that the resulting mixture was less viscous. The curing agent was then added and the mixture was placed in a vacuum so that the air bubbles could be removed. The mixture was then poured into the mold along the side of the mold so as to avoid further air bubble formation in the specimen. The first layer was then allowed to cure for 24 hours and the process was repeated for the second layer. In total, five layers were used to complete the specimen.

Once the completed specimen was cured and taken out of the mold, the dimensions and fiber orientation were measured. The parameters of the specimen are: $L = 3.81in, \alpha = 26.39°, a = 0.475in, b = 0.7in, \theta_1 = 9°, \phi_1 = 49°$. The exact radial location of the grating was determined as explained later in section 4.4.

Fig. 4.2 shows the grating (Corning Inc.) spectrum before and after embedding in the epoxy specimen. One observes the following points:

- No secondary peaks are observed in either spectrum. This indicates that during fabrication, the grating was chirped through a "dc"index change.
- The epoxy solidification process resulted in a non-uniform compressive residual stress along the grating that resulted in a shift of the peak to the left and a slight increase in bandwidth of the peak.

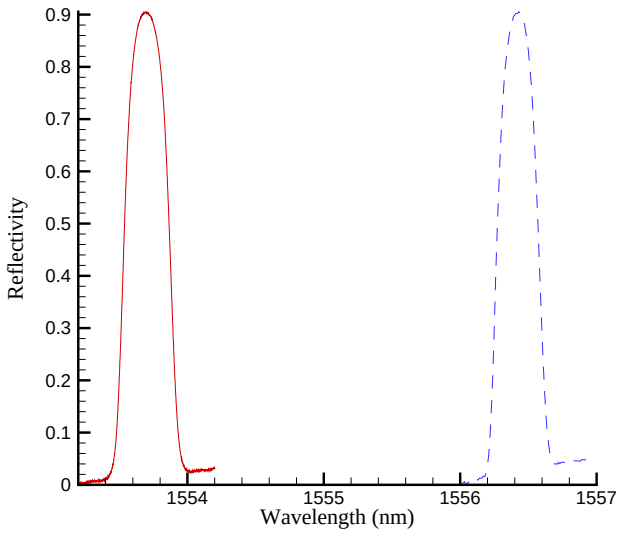

Figure 4.2: Reflection spectra of Bragg grating sensor. Dotted line represents spectrum before embedding in epoxy specimen and solid line represents spectrum after embedding.

4.3 Experimental Setup

The drawings of the loading frame used are given in Appendix A. In order to apply a cantilever boundary condition at the base of the cone, a tapered hole was bored into the L-frame so that the base fits tightly. The loading bar is guided so that it does not slip from the apex of the cone. Figures 4.3 and 4.4 show the mounted specimen in the loading frame. The base of the L-frame is fastened to the lower grip of the INSTRON 4400 (universal

testing machine) and the loading arm to the upper grip. A point load is applied to the apex of the cone through the displacement of the lower crosshead of the testing machine.

In order to estimate the maximum load that can be applied to the specimen and determine if the bonding between the layers of the cone is sufficient to consider the cone isotropic, a sample specimen without an optical fiber was loaded to fracture. The maximum load at failure was approximately 1500 lbs. The fracture occured at the clamped end of the cone indicating a strong bond between the epoxy layers. This bond was sufficient such that the specimen failed at the grip before delaminating internally. A maximum applied force of 800 lbs was therefore used for the following experiments.

The specimen was loaded quasi-statically. Figure 4.5 shows the block diagram of the experimental setup for measurements in transmission. The fiber entering the cone is connected to a tunable laser which is controlled by the computer. The fiber exiting the cone is connected to a photodetector. Labview 6.0 was used to control the laser output and to collect the data from the DAQ card. The load was increased from $0 - 800$ lbs and the specimen was loaded so that the grating is in compression.

4.4 Experimental Results

This section presents and analyses the sensor response during quasi-static loading of the specimen. The sensor spectra obtained at zero loading before and after the loading cycle matched well indicating that there is no permanent damage to the grating, and that the specimen and optical fiber remained in the elastic regime. Figure 4.6 shows the reflection spectra for the embedded grating as the conical specimen is loaded from $0 - 800$ lbs. One observes the following characteristics:

- a shift in the peak to the left with applied load indicating the grating is loaded in compression;
- an increase in bandwidth with applied load indicating a non-uniform strain along the grating;
- a decrease in maximum reflectivity indicating non-uniform applied strain and/or bending losses;

Figure 4.3: The loading frame mounted in the tensile loading machine. Also visible are optical fiber leads from the specimen.

Figure 4.4: The conical epoxy specimen mounted in the loading frame. Also visible is the loading arm held in the grips of the loading machine.

- lack of secondary peaks indicating a weak or insignificant quadratic variation of strain along the length applied to the grating.

Figure 4.7 plots the shift in wavelength at maximum reflectivity (linearly related to the average strain in the grating) vs. load. One observes that the relationship is piecewise linear with a change in slope at approximately $100lbs$ and $300lbs$. The change in slope at $100lbs$ is probably due to plastic deformation occuring at the loading point. This was visible afterwards as the loading bar point of contact had indented the epoxy cone. The change in slope at $300lbs$ is most likely due to line contact between the specimen and entire surface of the loading arm. Therefore, the true load-strain relationship was calculated from the slope of Fig. 4.7 in the applied loading range $300lbs - 800lbs$.

To determine the grating properties: the length, L, and $\delta n_{eff}(z)$, the grating spectrum before embedding was simulated using the Runge-Kutta method of section 3.1. A "bell"curve type distribution for $\delta n_{eff}(z)$ was assumed along the grating as shown in Fig. 4.8 (a) . The properties of the grating obtained are $L = 6.25mm$, $\delta n_{eff}(z) = 2.5\times10^{-04}$exp[-$8.6(z/L)^2$], $n_{eff} = 1.46$, and $\lambda_B = 1556.42nm$. Figure 4.8 (b) plots the experimentally

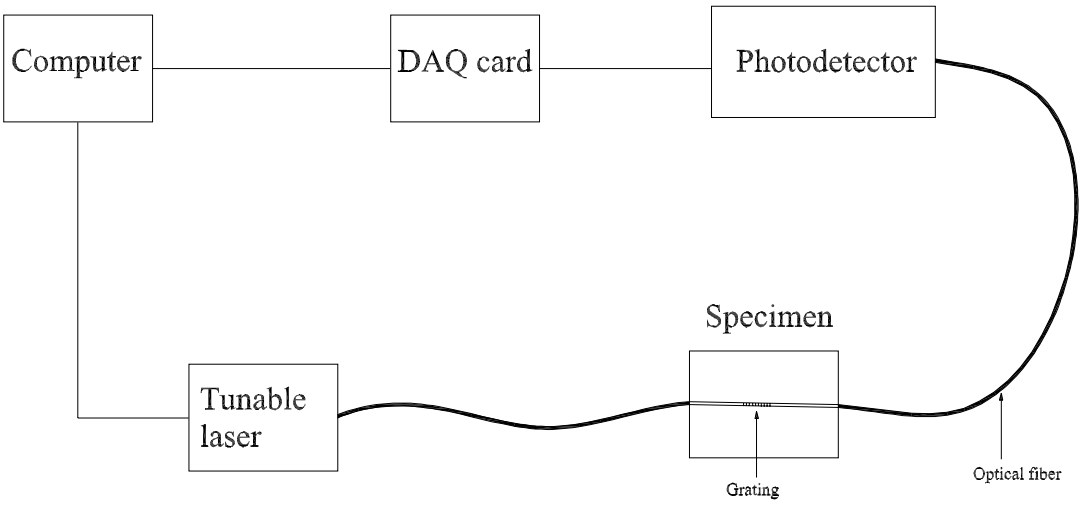

Figure 4.5: Block diagram of the experimental setup.

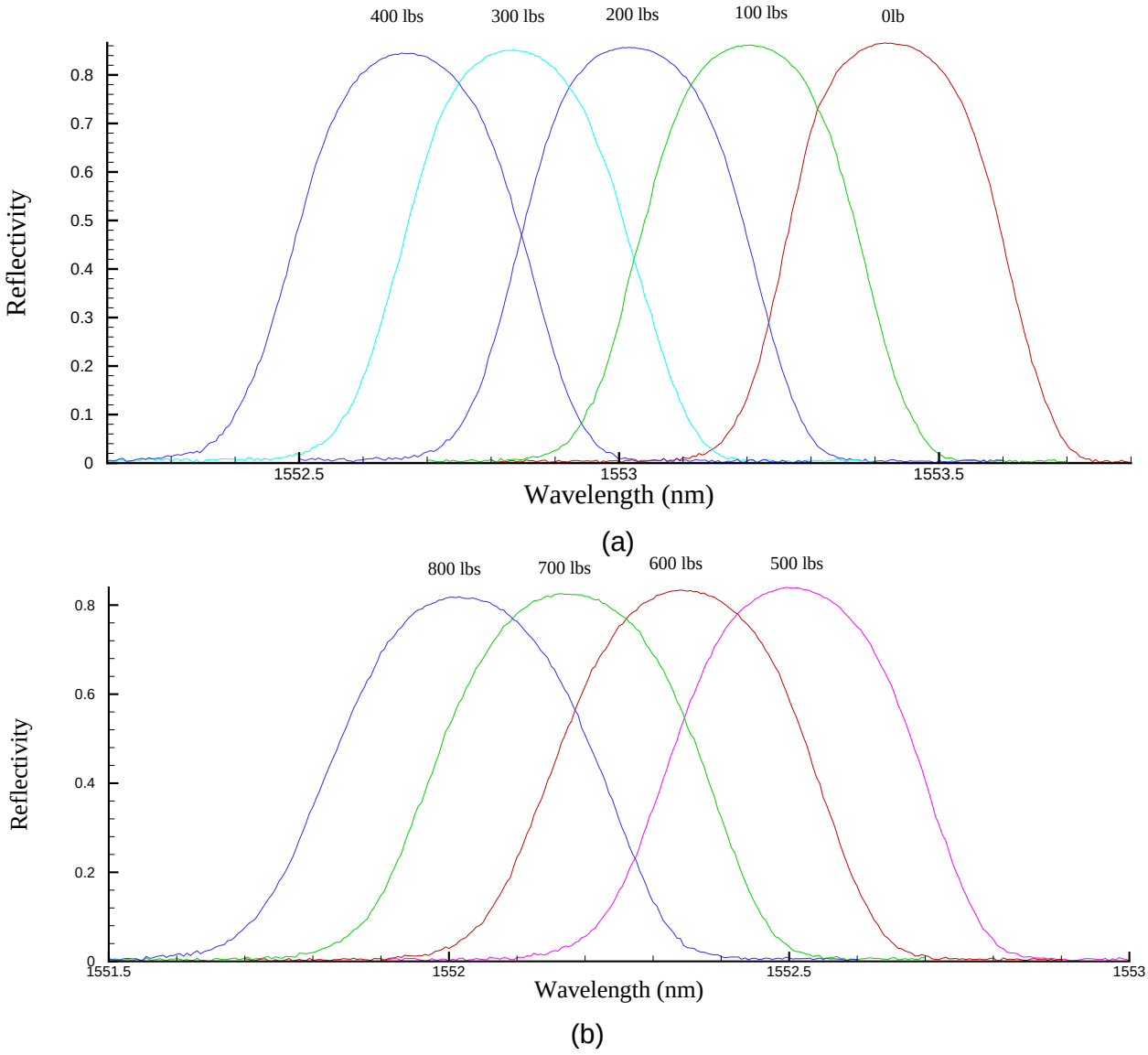

Figure 4.6: Reflection spectra of sensor as it is loaded from: (a) $0-400$ lbs, and (b) $500-800$ lbs in steps of 100 lbs.

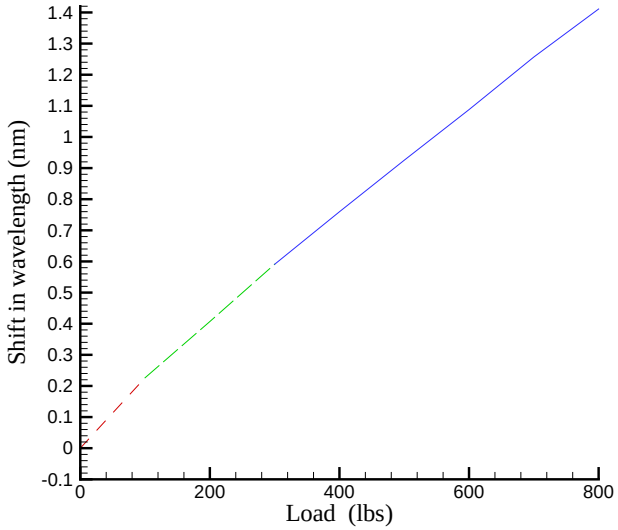

Figure 4.7: Variation of shift in wavelength of maximum reflection with applied load. Dashed line indicates load region before true load-strain relationship. Solid line indicates linear load region used for determination of grating location.

obtained and simulated grating spectra assuming the above variation of δn_{eff}.

In order to fit the experimental spectra with the cone solution, the cantilever condition was replaced by an applied pure shear and pure bending condition. The applied load was also transformed from the plane $r = a$ to the apex. The radial strain (i.e. the axial strain along the grating) is the sum of the radial strain due to the applied bending moment and shear. The properties of the epoxy specimen were assumed to be $E = 3500MPa$ and $\nu = .33$ [12]. As θ_1 and ϕ_1 for the fiber was known, the applied load and r were varied to obtain the required shift in the wavelength of maximum reflectivity for a load of $320lbs$. This yielded a grating location of $r = 1.9in$. Next, the location of the grating was fixed and the load varied to fit the experimental spectra. The shift in the peak i.e. the average axial strain along the grating, matched well with the experimental data, but the bandwidth did not match. Therefore, the form of the strain distribution along the grating was not that predicted by the exact cone solution. One of the reasons might be due to the assumption in deriving the exact strain field, i.e. the effect of the applied load decreases further away from the apex.

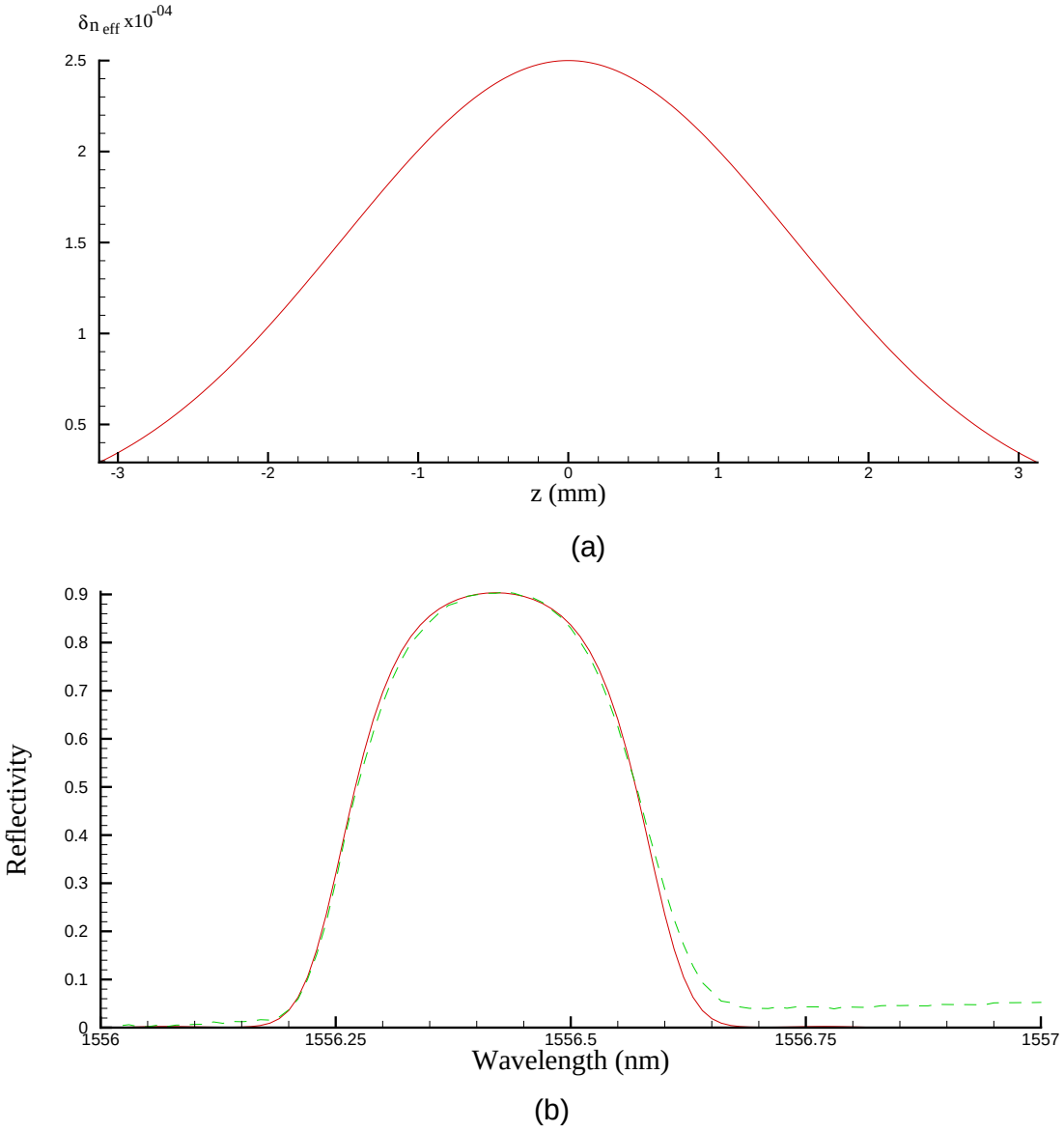

Figure 4.8: (a) Variation of $\delta n_{eff}(z)$ applied assuming "bell"curve type distribution. (b) Reflection spectra of the grating before embedding in the specimen. Dashed line represents experimental spectrum and solid line represents simulated spectrum.

Therefore, to calculate the strain distribution along the grating, the experimental spectra were simulated using the following approximation to the axial strain,

$$\epsilon(z) = a_0 + a_1 z + a_2 z^2 \tag{4.3}$$

where, z is the coordinate along the axis varying from $-L/2$ to $L/2$. Figures 4.9 and 4.10 show the experimental and simulated spectra as the applied load is increased from 0 to $800lbs$ using the assumption of Eq. (4.3). One observes that there is a loss in reflectivity only in the region near the maximum reflectivity. Figure 4.11 plots the calculated constants with load and the resulting strain distribution along the grating. One observes that:

- the constants a_0, a_1, and a_2 are linear with load after $300lbs$ as observed in Fig. 4.7;
- although a quadratic form of the strain distribution is assumed, the magnitude of the quadratic term is small, consistent with the observations from Fig. 4.6.

The % bending loss was calculated as given below,

$$\%bending - loss = \frac{r_s - r_e}{r_s} \times 100 \tag{4.4}$$

where, r_s is the simulated reflectivity, and r_e is the experimentally measured reflectivity. Figure 4.12 plots the % bending loss vs wavelength for several values of applied load. One observes that the bending loss is a non-linear function of load as expected. A maximum loss of 2.5% was observed at a load of $800lbs$.

The experimental spectra were fitted with simulated spectra by incorporating the bending loss function mentioned in Chapter 3. Since the length of the grating is small, a constant curvature was assumed along the grating. The bending loss function from section 3.2 is given by,

$$\Delta P(\lambda, z) = (\kappa f(\frac{1}{r})hz)^2 \tag{4.5}$$

where, $f(1/r)$ is a function depending on the fiber curvature. f is varied for each load so that the simulated spectra fits with the experimental spectra. Figure 4.13 shows the simulated and experimental spectra for various loads after including the bending loss function.

Figure 4.14 shows the variation of f with load and the different polynomial fits for the variation. The best fit is obtained with the third degree polynomial. Since the radius of curvature is varying linearly with load, the coefficient in the bending loss function varies cubically with the radius of curvature. Thus, we have demonstrated the variation of bending loss with radius of curvature.

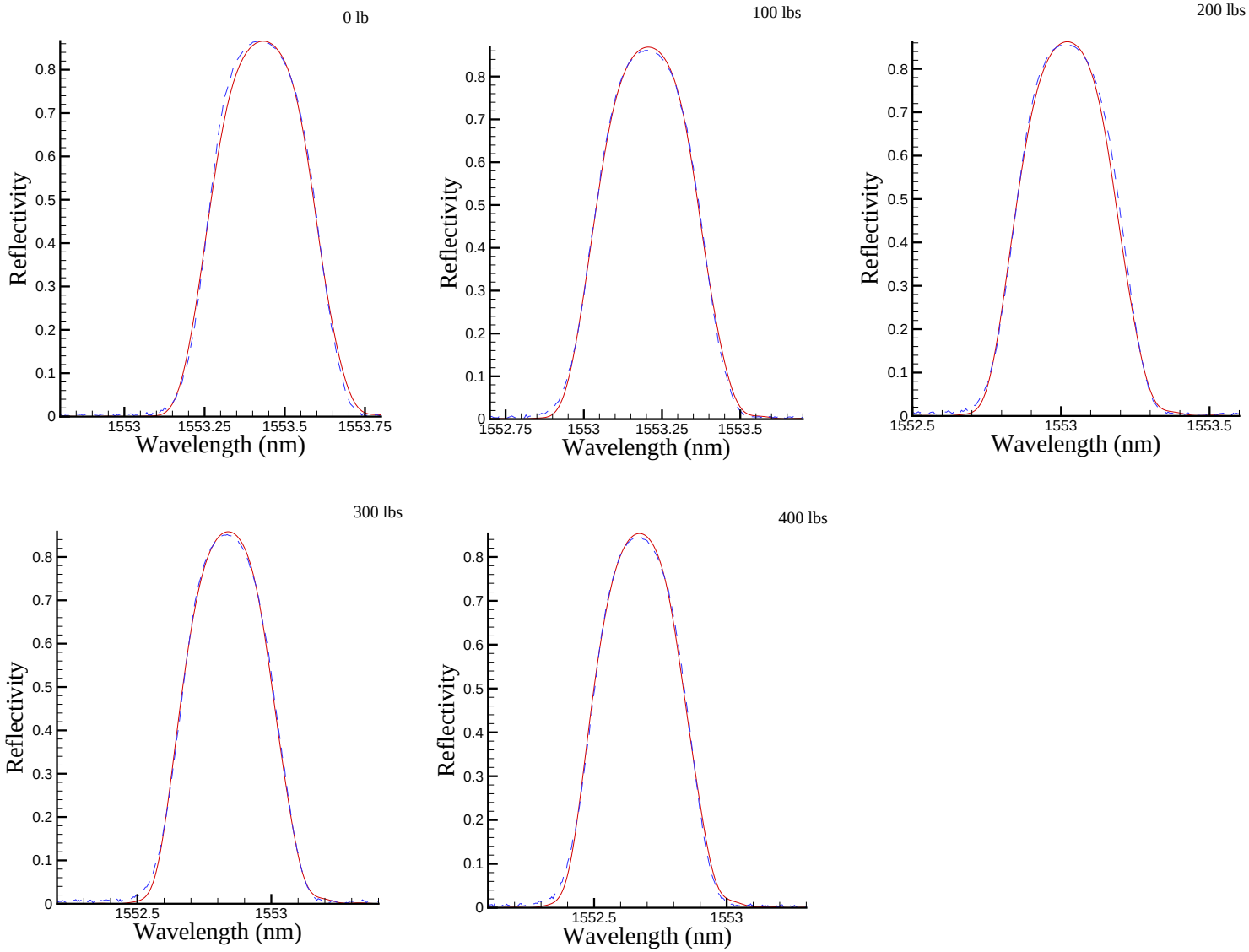

Figure 4.9: Reflection spectra for the applied load range of 0 to 400lbs. Dashed line represents experimental spectra and solid line represents the spectra simulated not including the bending loss function.

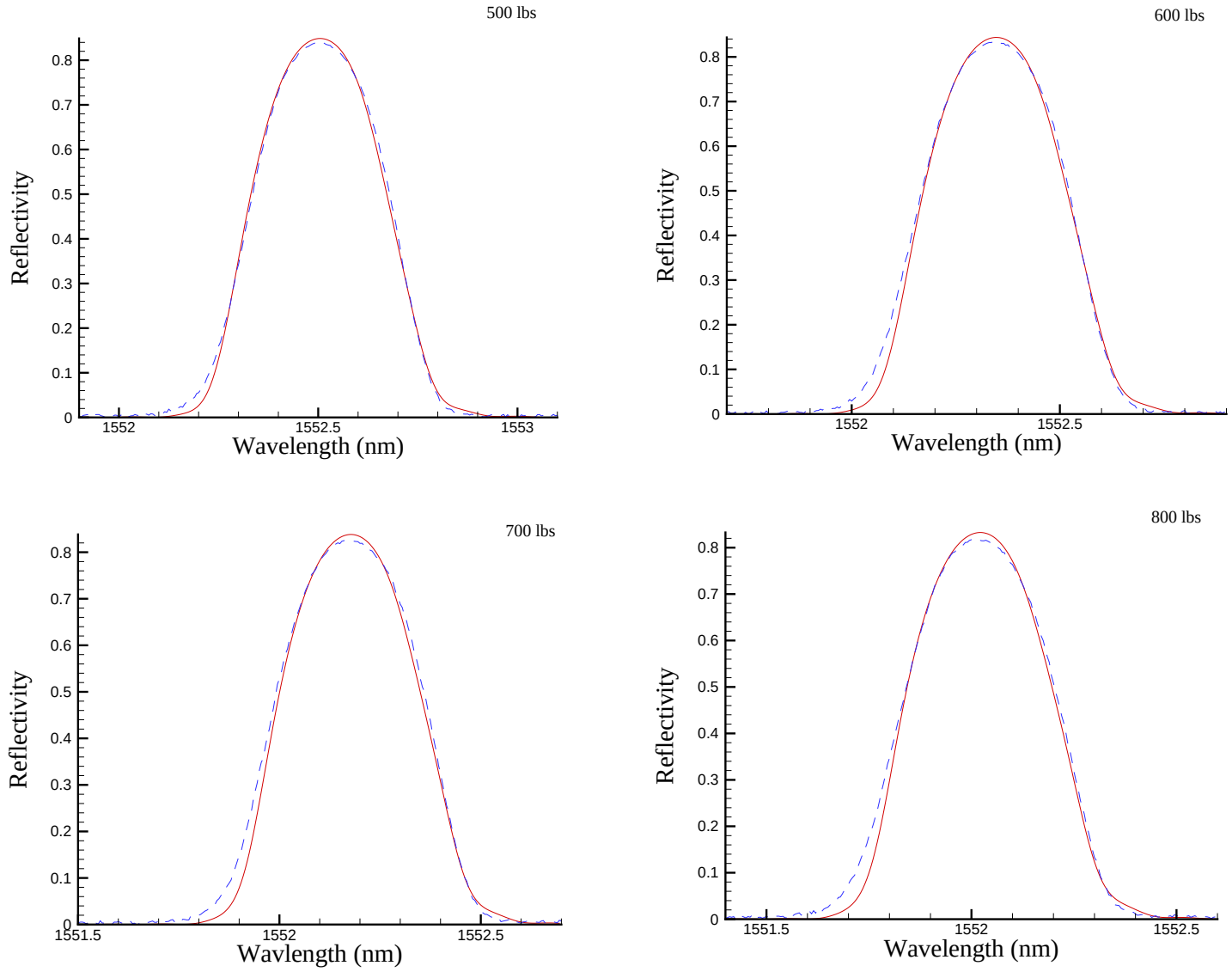

Figure 4.10: Reflection spectra for the applied load range of 500 to 800lbs. Dashed line represents experimental spectra and solid line represents the spectra simulated not including the bending loss function.

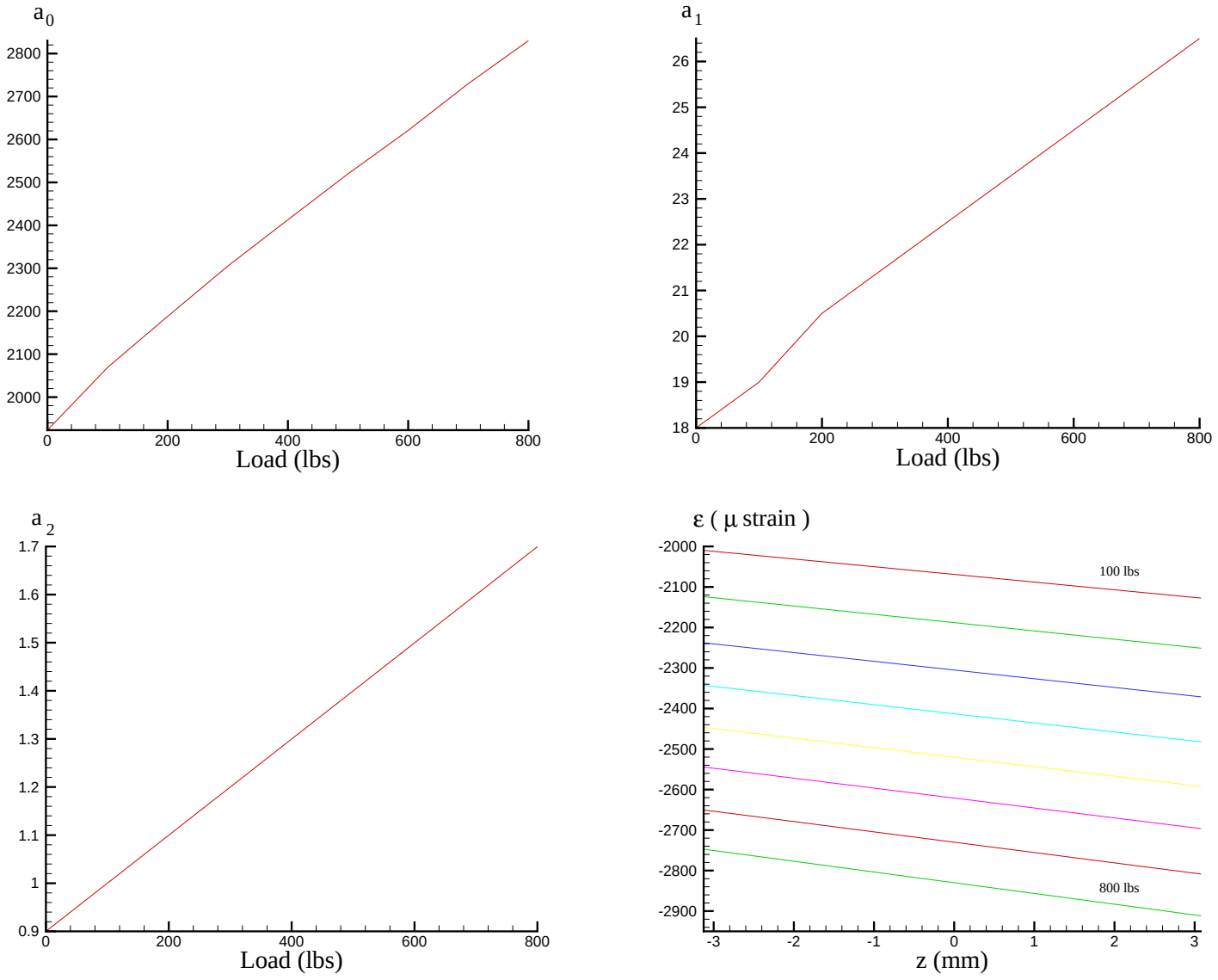

Figure 4.11: Variation of spectra fitting constants with applied load. Also shown is the strain distribution along the length of the grating for the applied load obtained from the fits.

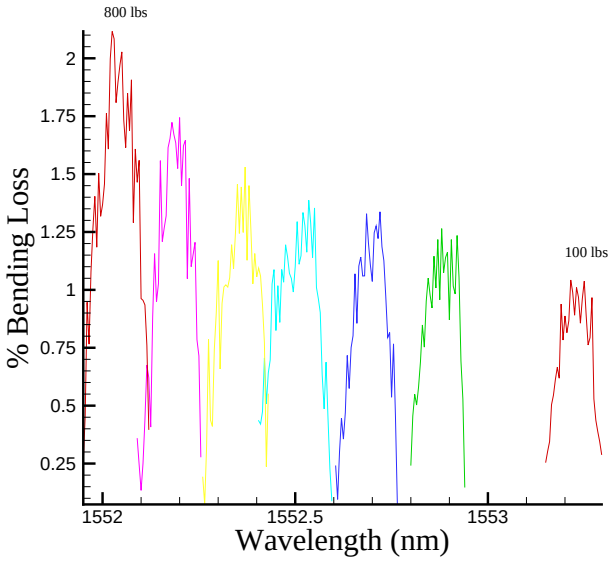

Figure 4.12: Variation of % bending loss with wavelength for different applied loads.

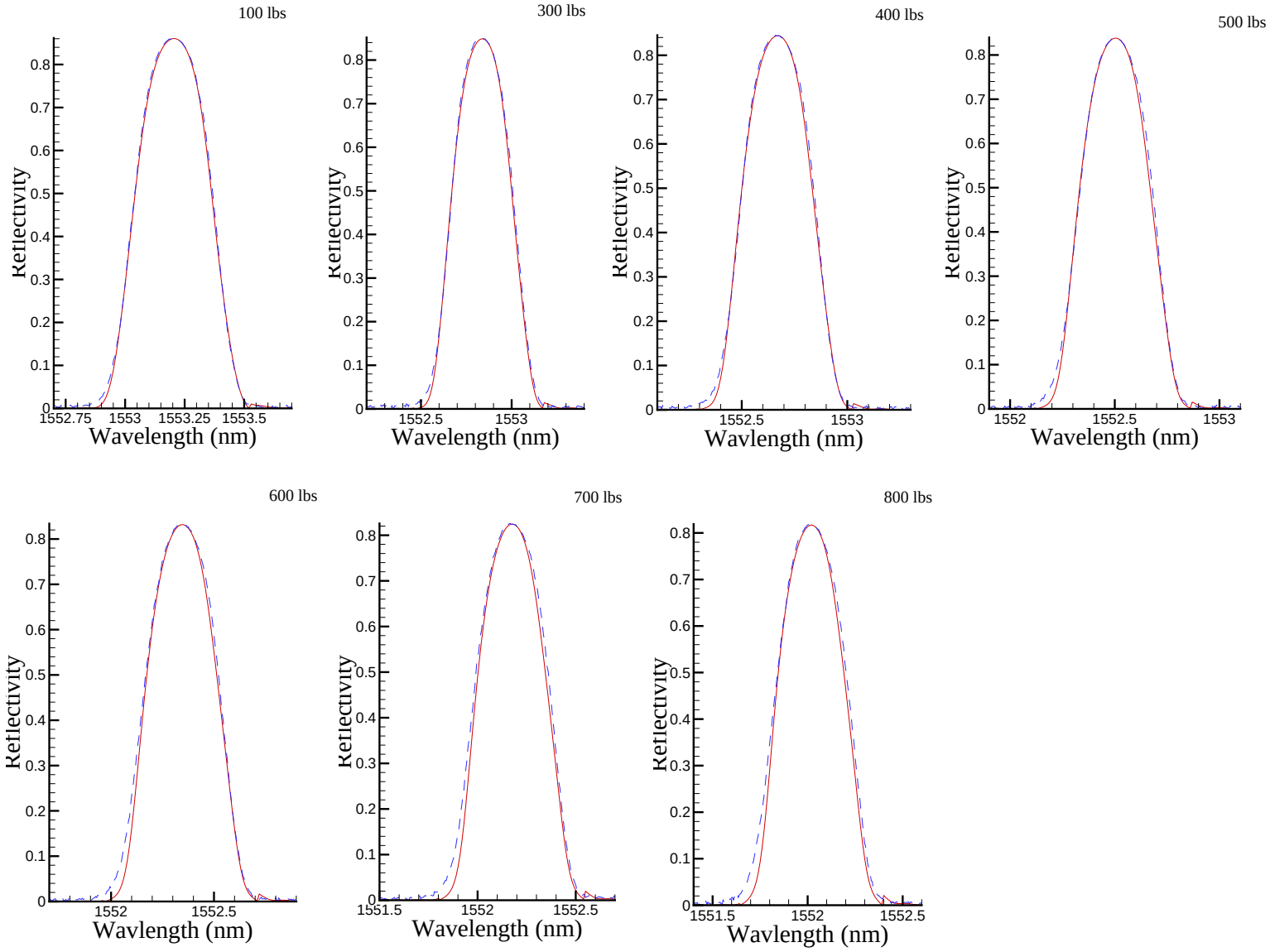

Figure 4.13: Reflection spectra for load varying from 100 to 800*lbs* after including the bending loss function. Dashed line represents experimental spectra and solid line represents simulated spectra

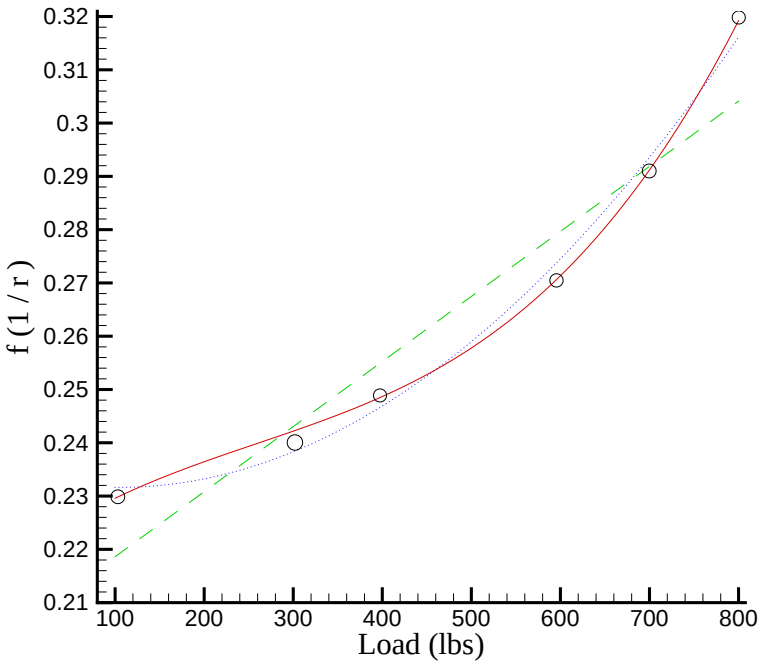

Figure 4.14: Different degree of polynomial fit for the variation of the function f with load. Solid circles represents the value f obtained from the fit to experimental data. Dashed line represents a linear polynomial fit, dotted line represents a quadratic polynomial fit, and solid line represents a cubic polynomial fit.

Chapter 5

Simulation of unidirectional composite with embedded sensors

The aim of this chapter is to efficiently simulate the response of sensors embedded in a unidirectional composite subjected to axial load with a propagating transverse crack. Both the effects of axial strain and bending on the sensor are considered when important. The strain field required for the sensor response is obtained from a finite element analysis and/or shear-lag theory approach, depending on the location of the sensor relative to the crack. In the first section, the limits of the shear-lag theory are found by comparing results with the finite element analysis. Using these limits we develop an algorithm to simulate sensor response depending on the location of the sensor. In the second section, several sensors are considered in a single fiber and their response is simulated for different crack lengths. In the final section, the application of this model to co-planar multiple cracks is evaluated.

5.1 Calculation of fiber stresses via shear-lag theory and finite element analysis

In order to compare the shear-lag theory and FEA models for later calculation of the sensor responses, a specific composite geometry was chosen. The geometry used is shown in Fig. 5.1. We consider a twenty-one layer composite with each layer of thickness $1mm$ and a length $80mm$. The properties of the matrix and fiber layers are: $E_f = 70\ GPa$, $\nu_f = .29$, $E_m = 3.5\ GPa$, and $\nu_m = .33$, that of glass and epoxy respectively. The first and last matrix layers are of thickness $0.5mm$ to preserve the matrix volume fraction of 0.5. The composite is subjected to a center crack in the plane $y = 0$. As an example, a center crack for which layers $9 - 13$ are broken is shown in Fig. 5.1.

Due to symmetry about the x-axis, only half the composite is required to be modeled. The full crack is modeled here in preparation for later geometries including multiple cracks. The composite is loaded in uniaxial tension such that $\sigma_f = 1.0MPa$ at the boundary $y = 40mm$. Since strain continuity is enforced between the fiber and matrix layers, i.e. $\epsilon_m = \epsilon_f$, the matrix stress at the boundary $y = 40mm$ is given by [2],

$$\sigma_m = \frac{E_m}{E_f}\sigma_f \tag{5.1}$$

Using the shear-lag theory, the boundary conditions given in section 2.3 are applied to solve for the thirty nine unknown constants (i.e. the crack surface is free, the average axial stress in each layer asymptotes to the applied load, and the average vertical displacement on either side of crack at $y = 0$ is zero). To solve for the remaining unknown constant we assume that the first layer is far away from crack tip and hence apply $< \sigma_y^{(1)} >= E^{(1)}/E_f$ at $y = 0mm$, i.e.

$$\sum_{j=1}^{n-1}(a_j + b_j)\frac{\psi_{j,1}}{t_1} = 0 \tag{5.2}$$

Since the problem geometry and loading are both symmetric, one expects symmetric results, i.e. that the average axial stresses and interfacial shear stresses are symmetric about layer 11. Figures 5.2 and 5.3 plot the average axial stress obtained using the above boundary conditions for two different crack lengths. Clearly, the resulting axial stress fields are not symmetric. Consider the axial stress distributions for layers 14 and 8 in Fig. 5.2. These are the two fiber layers located on either side of the crack tip. Far away from the crack the average axial stress in both layers approach the applied loading. Further, it was verified that

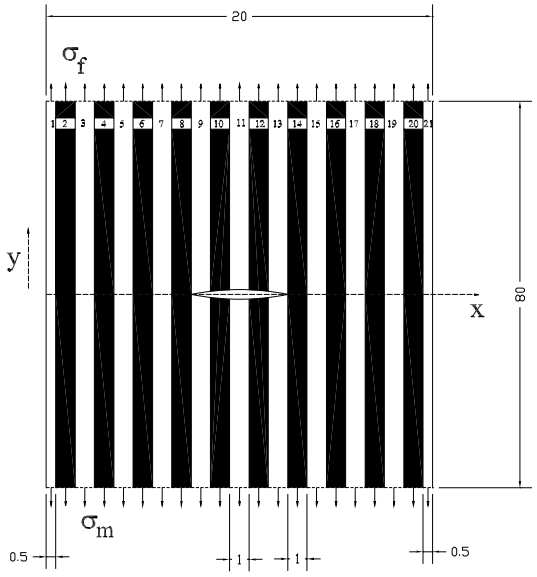

Figure 5.1: Unidirectional composite model composed of 21 layers and a center crack, here shown extending through layers $9-13$. All dimensions are in mm. Drawing not to scale.

both stress fields satisfy the differential equation of equilibrium and boundary conditions to within the numerical error of the problem. Therefore, there are two apparent solutions for the same shear-lag model. One solution approaches the applied loading from above and other from below, i.e. one has a stress concentration at $y = 0$ and the other demonstrates reduced stresses at $y = 0$. Since the composite is loaded in tension we expect a local stress concentration at $y = 0$ and therefore suppose that the former solution is correct.

After investigations, the primary reason for not obtaining symmetric plots was found to be the incompleteness of the eigenvectors for Eqs. (2.8) and (2.9). Consider the composite shown in Fig. 5.1. The average axial stress in layers 10 and 12 are given by,

$$< \sigma_y^{(10)} >= \frac{E^{(10)}}{E_f} + \sum_{j=1}^{n-1}(a_j e^{\lambda_j y} + b_j e^{-\lambda_j y})\frac{\psi_{j,10}}{t_{10}}$$
$$< \sigma_y^{(12)} >= \frac{E^{(12)}}{E_f} + \sum_{j=1}^{n-1}(a_j e^{\lambda_j y} + b_j e^{-\lambda_j y})\frac{\psi_{j,12}}{t_{12}} \tag{5.3}$$

Due to the symmetry conditions these average axial stresses should be equal, i.e. $< \sigma_y^{(10)} >=< \sigma_y^{(12)} >$, for all values of y. Since $E^{(10)} = E^{(12)}$ and $t_{10} = t_{12}$, the coefficients in front of the eigenvectors must be equal, therefore

$$\psi_{j,10} = \psi_{j,12} \qquad \forall j = 1, ..., n-1 \tag{5.4}$$

Thus, the 10^{th} and 11^{th} elements of each eigenvector must be equal. This requirement can be shown for all symmetric layers. Equation (5.4) leads to the following contradiction: Consider a (3×3) matrix with real and distinct eigenvalues. If one requires that the 1^{st} and 3^{rd} element of all eigenvectors to be equal then the eigenvectors have the following form:

$$\begin{bmatrix} x_1 \\ y_1 \\ x_1 \end{bmatrix}, \begin{bmatrix} x_2 \\ y_2 \\ x_2 \end{bmatrix}, \begin{bmatrix} x_3 \\ y_3 \\ x_3 \end{bmatrix}$$

One can obtain only two linearly independent eigenvectors of the above form. The third eigenvector is by definition linearly dependent on the other two. Thus the eigenvectors do not span the complete 3D space. Similarly, for the 21 layered composite considered above, only 11 eigenvectors would be linearly independent. However, for a matrix with real and distinct eigenvalues such as the matrix $[M_\sigma]$, the eigenvectors must be linearly independent. Therefore, the optimal shear-lag theory yields correct results only for non-symmetric composite geometries.

A second contradiction occurs when one considers the average axial stress in the center layer. Consider the differential equation of equilibrium for layer 11 of Fig. 5.1.,

$$\frac{d(t_{11} < \sigma_y^{(11)} >)}{dy} = \tau(x_{10}) - \tau(x_{11})$$

For symmetric results we require $\tau(x_{10}) = \tau(x_{11})$, therefore $< \sigma_y^{(11)} > = constant$. However, the axial stress in layer 11 must vary from zero at $y = 0$ to the applied load at $y = 40mm$.

Thus it is not possible to model one half of the composite with a center-crack using the optimal shear-lag theory of Nairn and Mendels. Fortunately, for the crack location chosen, due to the vertical symmetry model it is only necessary to model one quarter of the composite. For the single crack geometry located far from the edge boundaries, the axes can always be adjusted such that the model is reduced as described above, however this requirement will present difficulties for the multiple crack case considered later. The center-cracked composite of Fig. 5.1 with $7-15$ layers broken was remodeled as a composite with 11 layers with $1-5$ layers broken. The respective boundary conditions were applied as given in section 2.3.

Simultaneously, Finite Element (FE) analysis of the center-cracked composite was performed using ANSYS. Only one fourth of the composite was modelled due to the symmetries. Eight noded quadrilateral elements were used. Plane stress conditions due to the

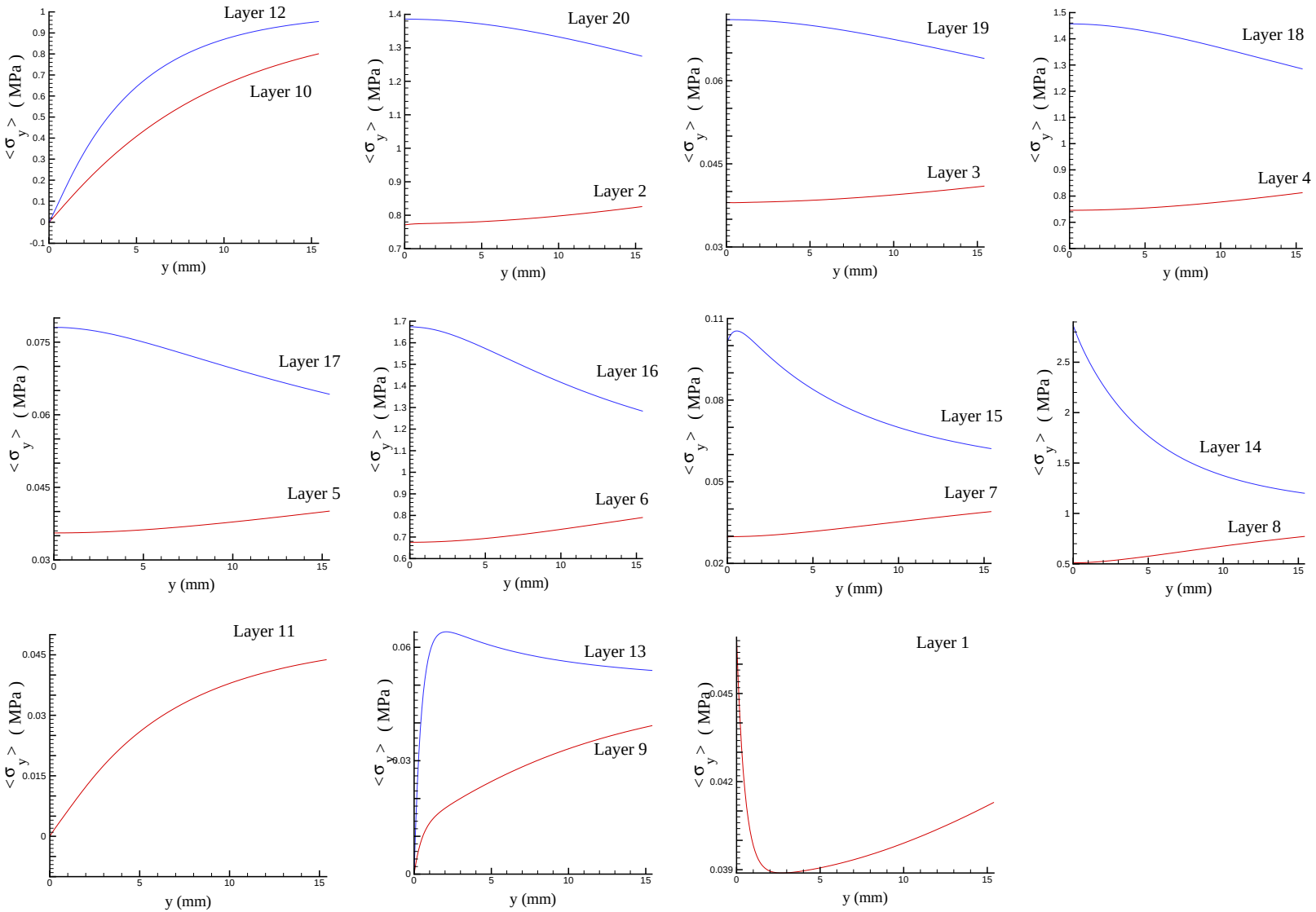

Figure 5.2: Average axial stress in each layer for center crack of length layers $9-13$ broken calculated via shear-lag theory. Layers at symmetric locations are plotted on the same graphs. Note, the stress in layer 21 is not calculated.

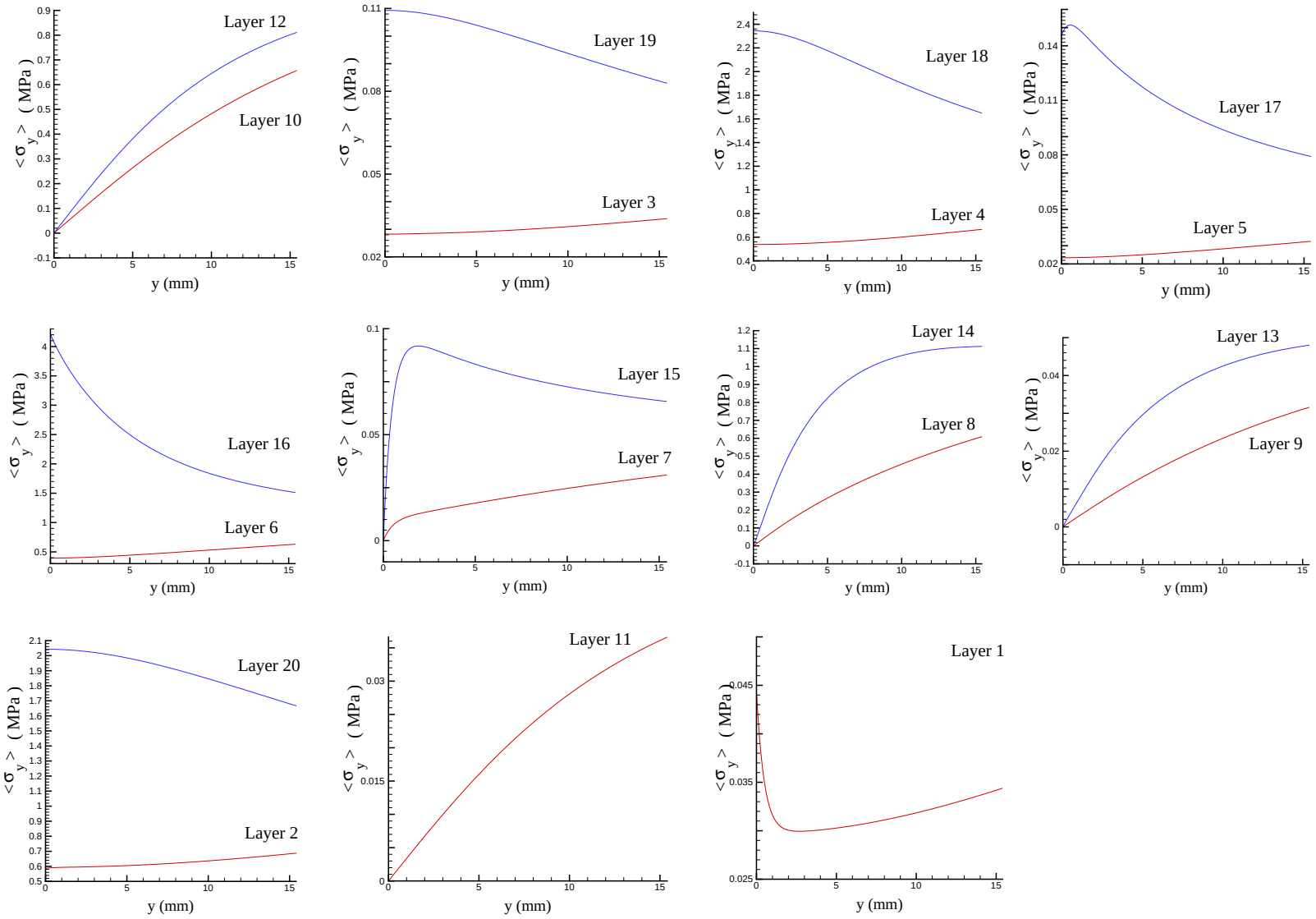

Figure 5.3: Average axial stress in each layers for center crack of length layers $7-15$ broken calculated via shear-lag theory. Layers at symmetric locations are plotted on the same graphs. Note, the stress in layer 21 is not calculated.

composite thickness of $1mm$ were applied as shown in Fig. 5.4. The same element type with different material properties were used for the fiber and matrix layers. Perfect bonding between the fiber and matrix layers was enforced through displacement continuity for all nodes along the interface between matrix and fiber layers. A relatively fine mesh size of 200 elements along the layer length and 20 elements along the layer width was used for each layer as shown in Fig. 5.5. The applied boundary conditions are as shown in Fig. 5.6. The same loading was applied to the FE model as to the shear-lag composite model.

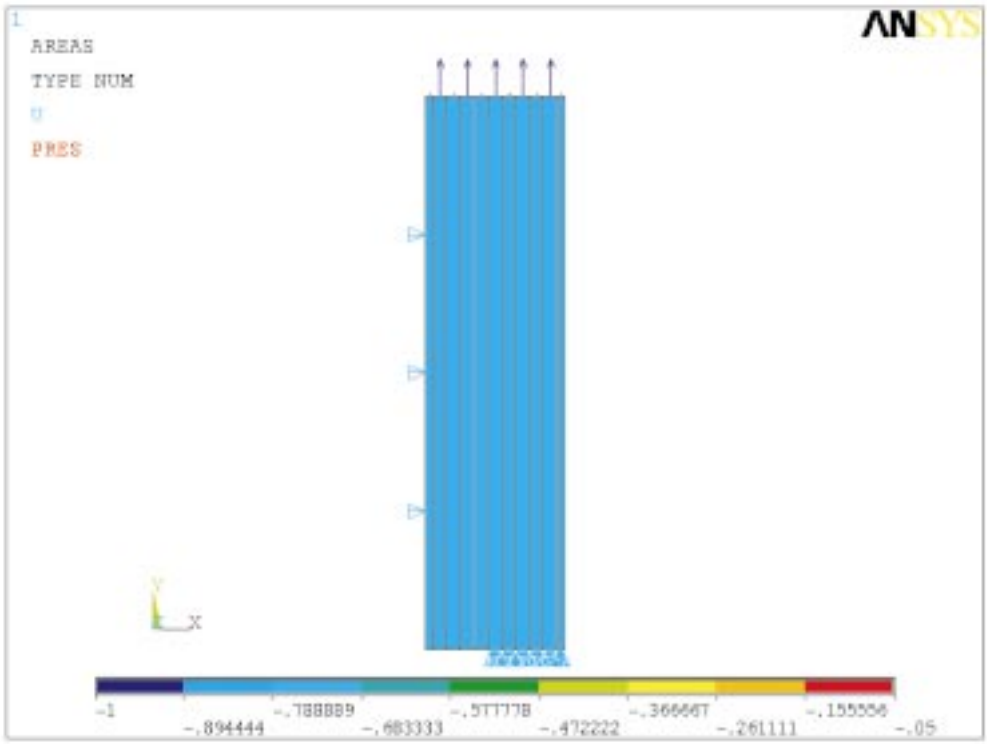

Figure 5.4: ANSYS model for 1/4 composite whose geometry is defined in Fig. 5.1. Symmetric boundary conditions are applied.

Figure 5.7 plots the comparison between FEA and shear-lag results for the average axial stresses, $< \sigma_y >$, in all layers of the twenty-one layered composite with a center crack traversing layers $7 - 15$. The difference in results from the shear-lag and FEA approach is mainly due to the assumption that the shear-lag theory models each layer as a 1-D spring element. Far away from the crack both the FEA and shear-lag theory asymptote to the applied load. Fig. 5.8 plots the interfacial shear stress between layers using both FEA and shear-lag theory. Here the primary difference is due to the fact that the shear-lag assumes

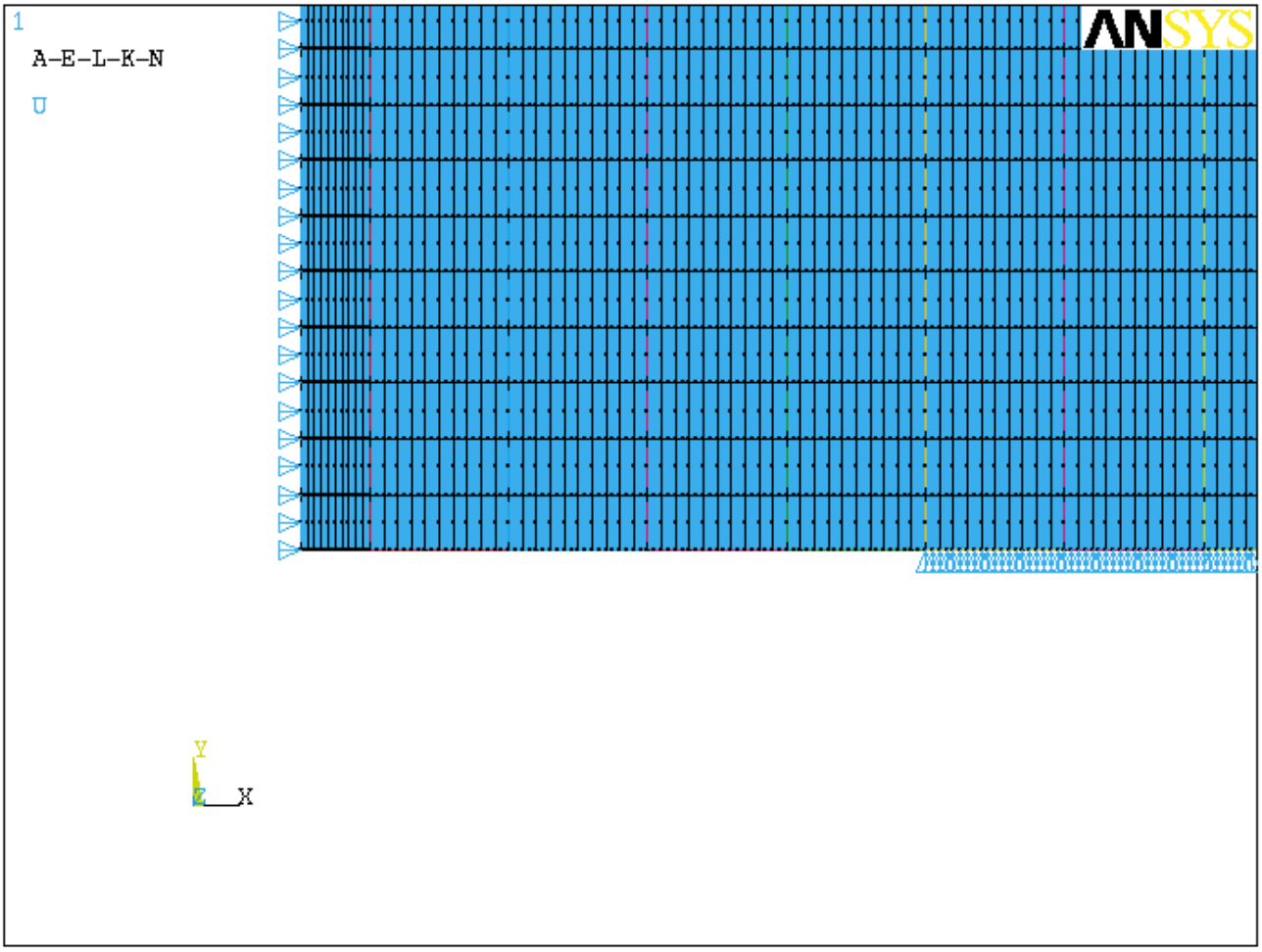

Figure 5.5: ANSYS model showing the elements used for the composite defined in Fig. 5.1 in the region of the crack tip.

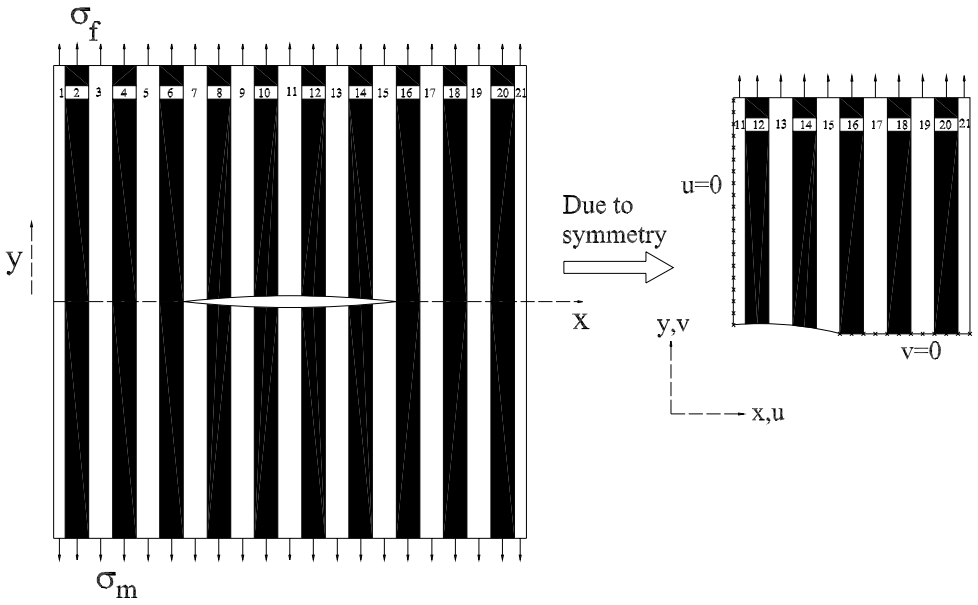

Figure 5.6: Boundary conditions for center cracked composite FE model. σ_m and σ_f are the remote stresses applied on the matrix and fiber layers respectively.

the shear stress in each layer to be a linear variation of the interfacial shear stresses on both sides of that layer.

These simulations have shown that the shear-lag theory yields good results for locations far from the crack tip. For locations close to crack tip FEA yields accurate results. Thus, we can use the shear-lag theory until damage occurs. Once the damage is indicated i.e. by a significant change in the form of the spectrum obtained from the sensor, we need to re-evaluate the sensor responses with FE model, including the effects of bending loss. We then use these measurements to estimate the location and size of damage.

5.2 Response of sensors due to a propagating tranverse crack

The aim of this section is to simulate the response of sensors embedded in a single fiber layer for different crack lengths approaching the sensor fiber. The strain field obtained from FEA is applied to the sensors for different crack lengths. Consider the composite shown in Fig. 5.1 with layers $7-15$ broken. Due to symmetry the composite is modelled using 11 layers with layers $1-5$ broken. The gratings are located at y=$0-5mm$, $15-20mm$, and

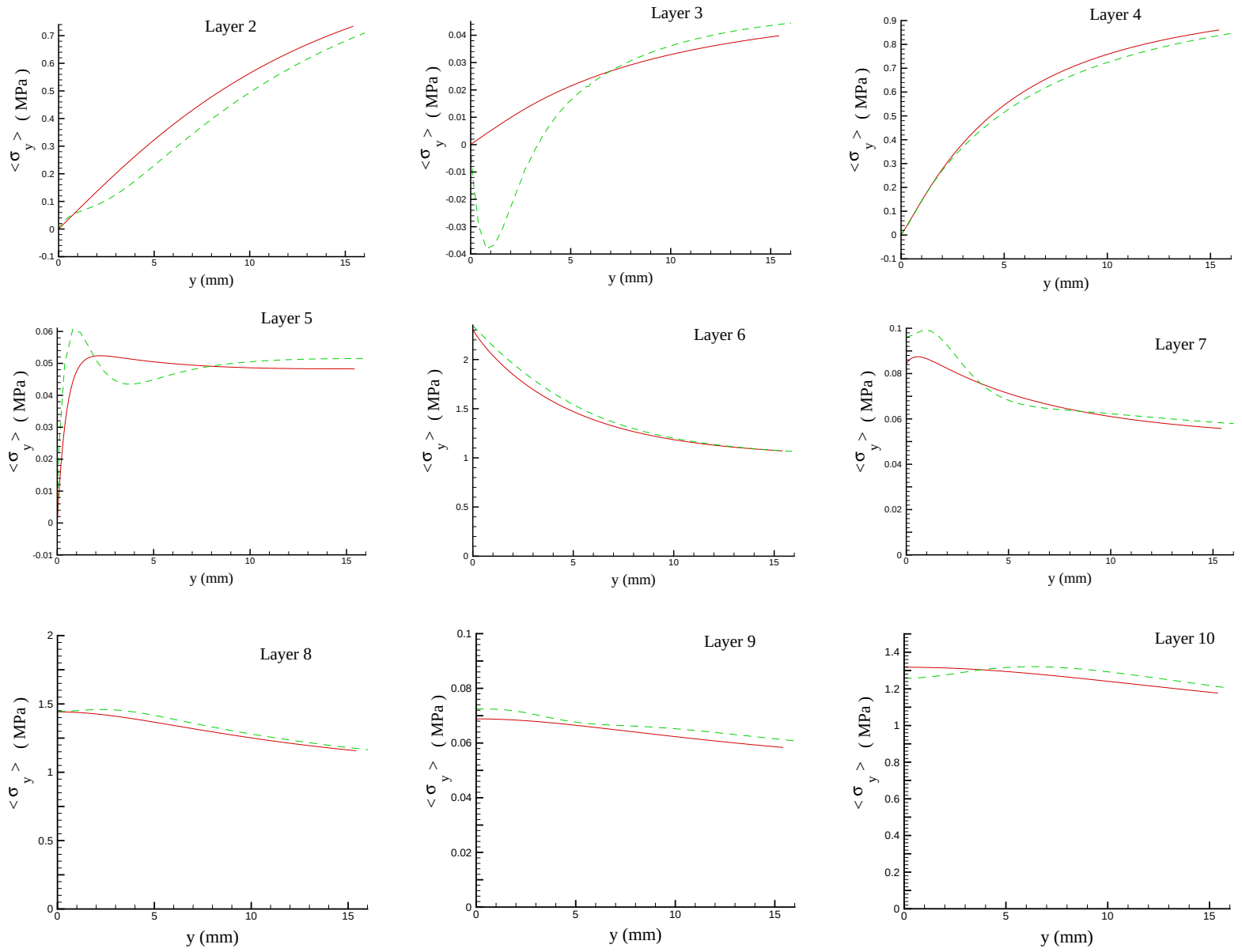

Figure 5.7: Calculated average axial stress in all layers for the center cracked composite. The results using shear-lag theory are plotted as solid lines, while the results from the finite element analysis are plotted as dashed lines.

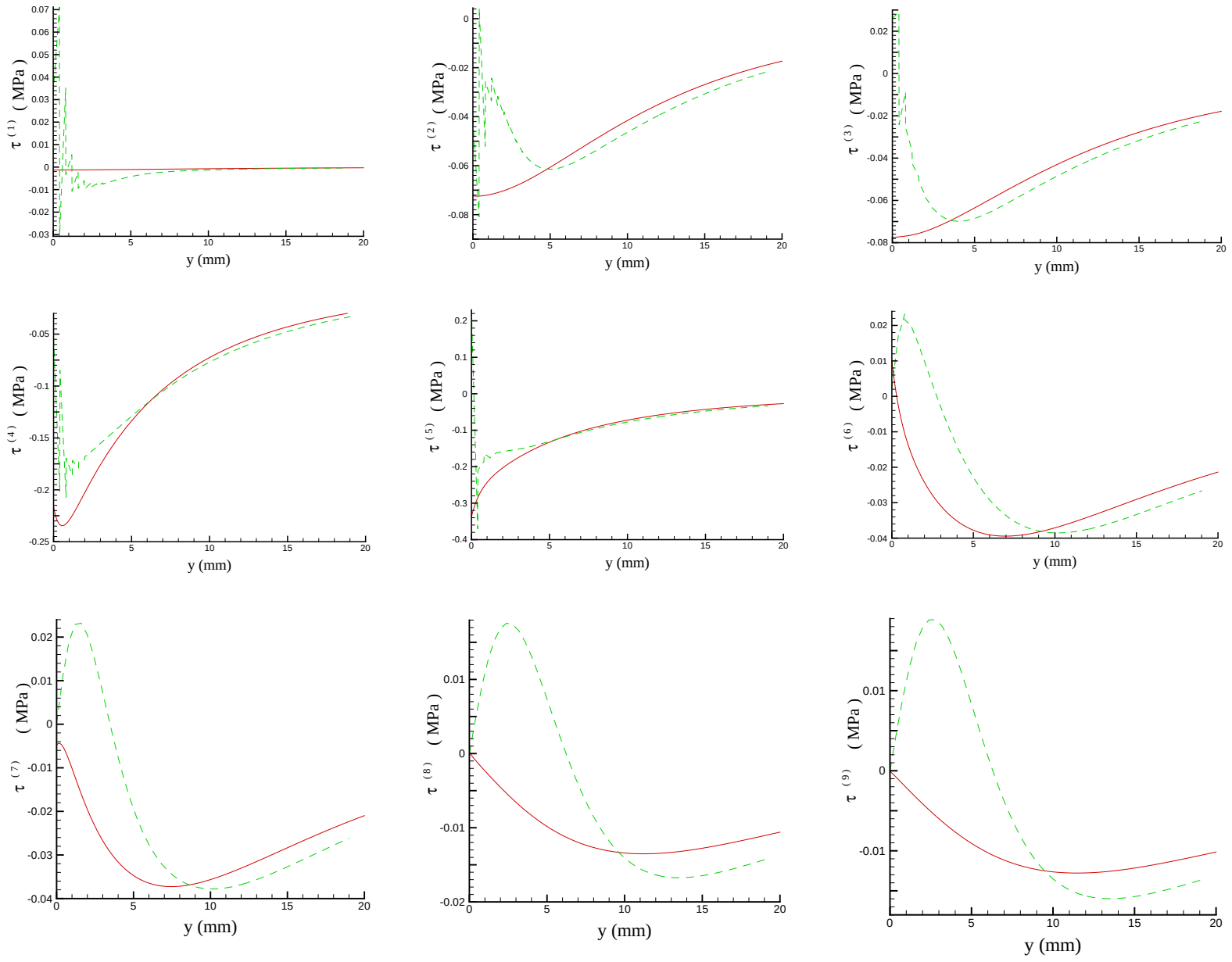

Figure 5.8: Calculated interfacial shear stress for the center cracked composite. The results using shear-lag theory are plotted as solid lines, while the results from the finite element analysis are plotted as dashed lines.

$30-35mm$ in layer 8 as shown in Fig. 5.9. These choices model the case of a sensor located close to crack, far from the crack, and in the transition zone between the two. Figure 5.10 shows the average axial stress in layer 8 obtained for different crack lengths. From Fig. 5.10 we observe that shear-lag theory overpredicts the axial stress as compared to the FEA for the average axial stress for all matrix layers near the crack tip and underpredicts for all fiber layers near the crack tip.

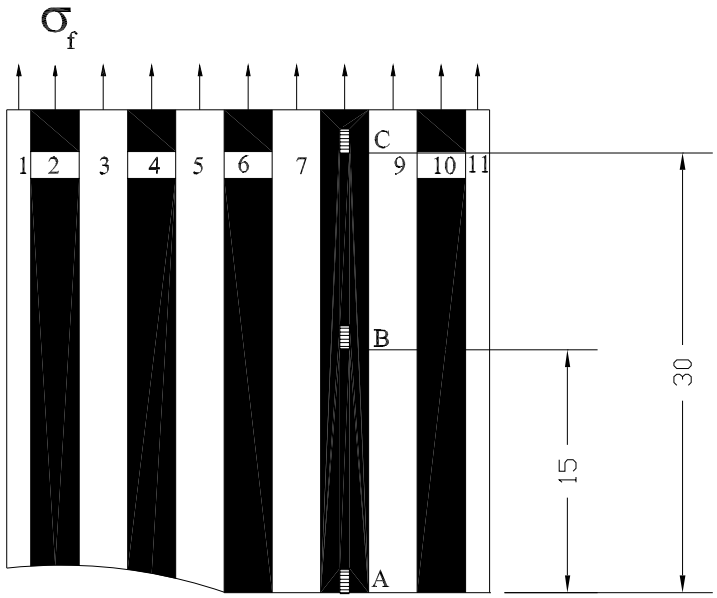

Figure 5.9: Locations of embedded gratings A, B, and C in modeled unidirectional composite (all dimensions in mm).

In order to simulate the grating response, the composite applied load σ_f is scaled such that a strain of 0.1% is applied to both the fiber and matrix layers. This applied load is considered to be a value at which some micro-damage might have occured in the composite, yet it would not have failed catastrophically. Figure 5.11 shows the average axial strain variation in each grating for different crack lengths obtained from the FE model. The strain field at each grating location for different crack lengths was fitted by a quadratic strain distribution. The above strain distributions were applied along the length of the grating, i.e. from $z = -L/2$ to $z = L/2$, where L is the length of the grating and the sensor response is simulated using the formulation of Chapter 3. Simulations were performed including and not including the bending loss as a function of local curvature of the fiber. Fig. 5.12 plots the obtained reflectivity of the gratings A, B, and C for the different crack lengths. In

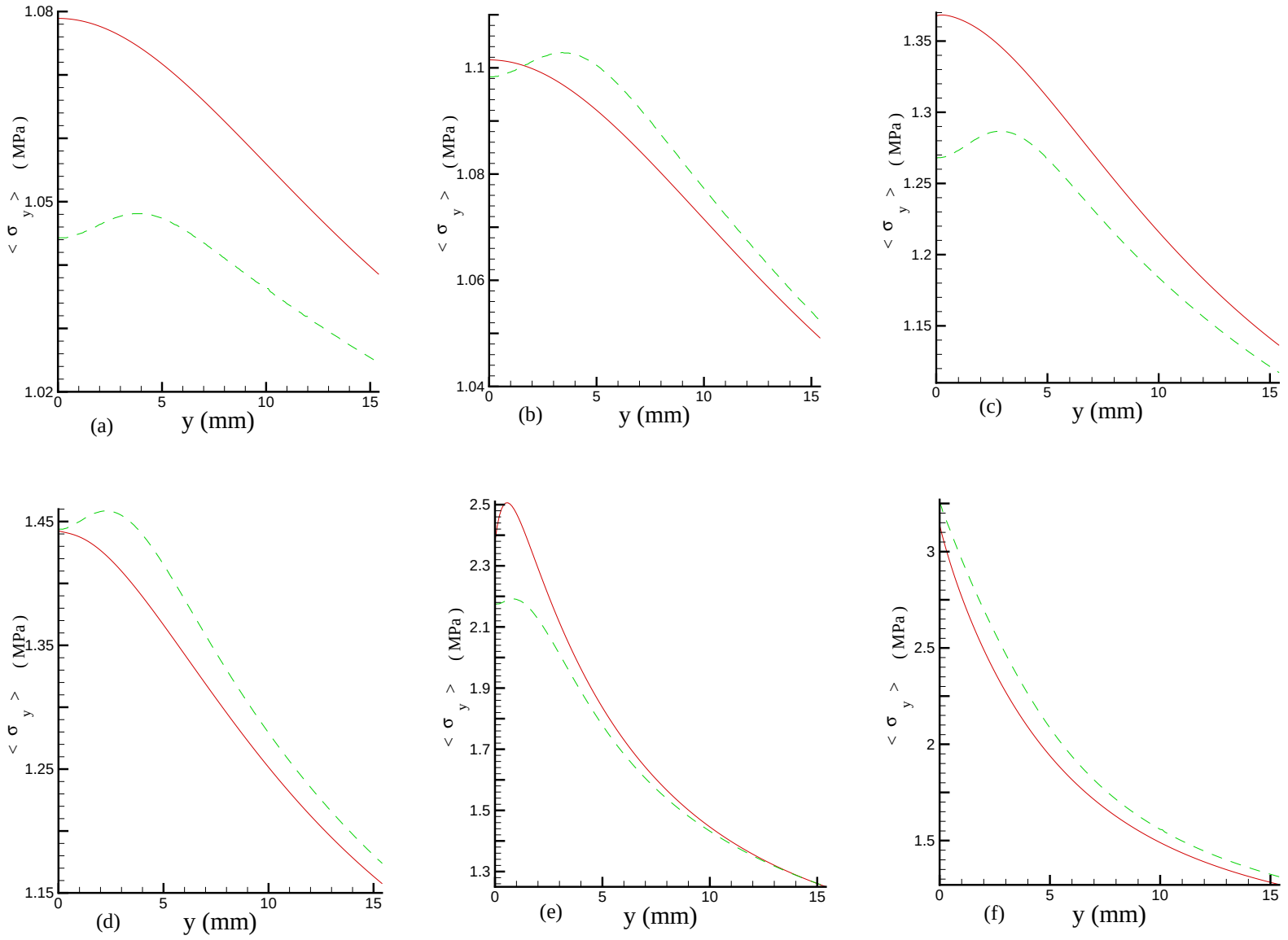

Figure 5.10: Calculated average axial stress $< \sigma_y^{(8)} >$ in layer 8 for different crack lengths: (a) layers 1-2; (b) layers 1-3; (c) layers 1-4; (d) layers 1-5; (e) layers 1-6; (f) layers 1-7. The results using shear-lag theory are plotted as solid lines, while the results from the finite element analysis are plotted as dashed lines.

the above simulations, the following grating properties were asssumed: $\delta n_{eff} = 2 \times 10^{-4}$, $L = 5mm$, $n_{eff} = 1.46$, and $\lambda_B = 1558nm$. When layers $1-3$ are broken the sensor is far away from the crack tip and thus the strain distribution in the grating is a constant or linear with a small slope. The bending loss is not significant. When layers $1-5$ are broken the strain distribution in gratings A, B, and C are approximately quadratic, linear and constant. The bending loss is significant in gratings A and B but is negligible in grating C. When layers $1-7$ are broken the grating A is next to crack tip and strain is approximately three times the applied strain. We observe that the bending loss is only present at locations of high strain gradients and in the peaks at larger wavelengths.

5.3 Application of model to composite containing multiple cracks

Naturally the future goal of a combined shear-lag/FEA model for sensor response would be to calculate the sensor response in a unidirectional composite containing multiple cracks. In this section, the feasibility of such an application is investigated. Since the shear-lag theory mostly easily models cracks in the same plane, we consider a thirty-one layered composite with a center crack and two other cracks symmetrically located on either side of the center crack as shown in Fig. 5.13. Due to symmetry only one fourth of the composite is modeled, i.e. fifteen layers with two cracks. We consider two cases: one case where the cracks are relatively close to one another and another case where they are farther from each other. Figures 5.13 (a) and (b) show the half composite geometry with the two modeled crack locations. As before, the composite is loaded such that $\sigma_f = 1.0\ MPa$ at $y = 40mm$.

The boundary conditions given in section 2.3 are applied to solve for the twenty seven unknown constants, i.e. that the crack surface is free, the average axial stress in each layer asymptotes to the applied load, and the average vertical displacement at $y = 0$ on either side of the crack is zero. Unfortunately, for the case of a fully embedded crack, the number of boundary conditions is always one less than the number of unknowns. Without further knowledge of the stress solution, one cannot solve the system. To solve for the remaining one unknown in this example, we force the axial stress in layer 8 at $y = 0mm$ to

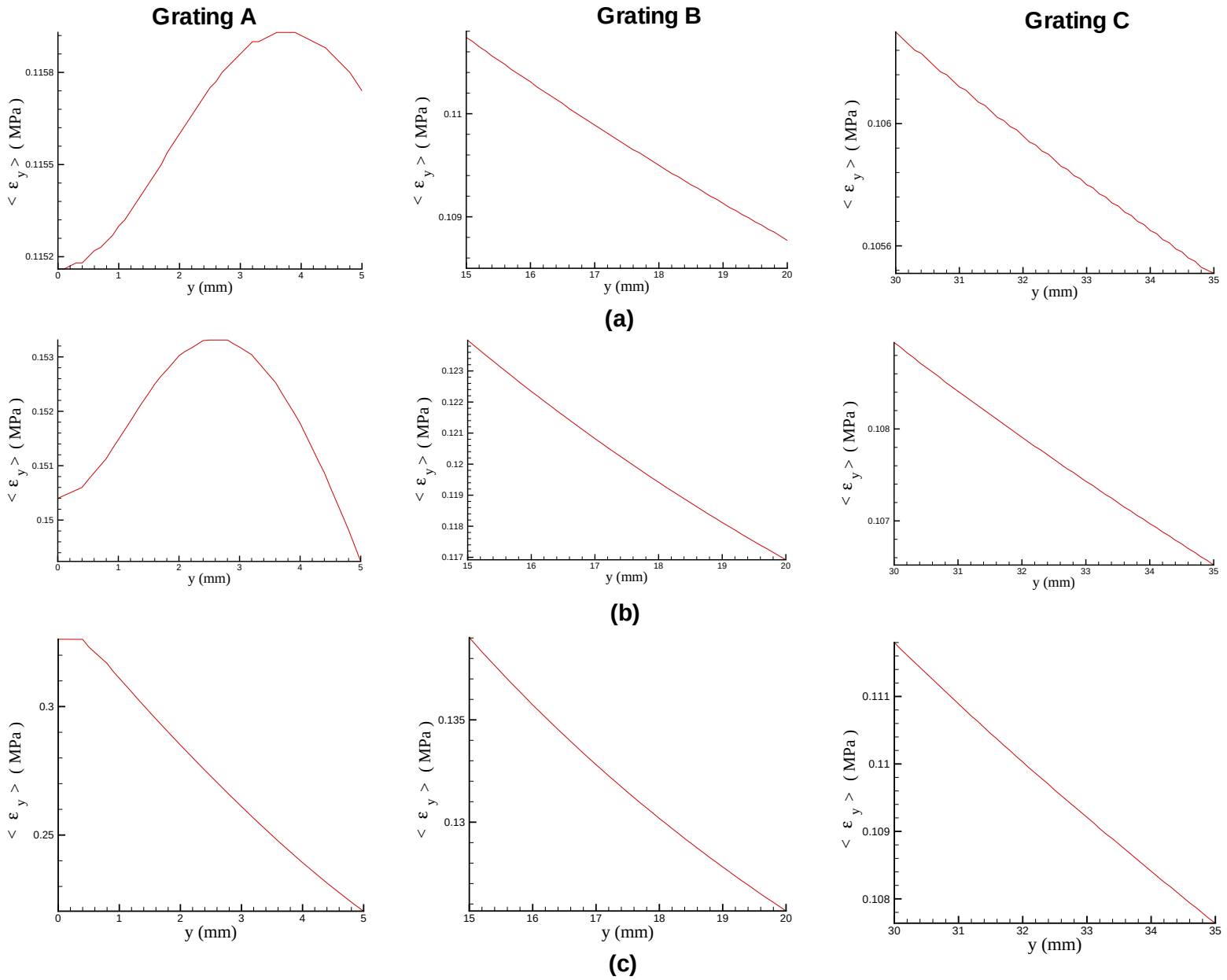

Figure 5.11: Average axial strain in gratings A, B, and C embedded in layer 8 for different crack lengths: (a) layers 1-3 broken; (b) layers 1-5 broken; (c) layers 1-7 broken.

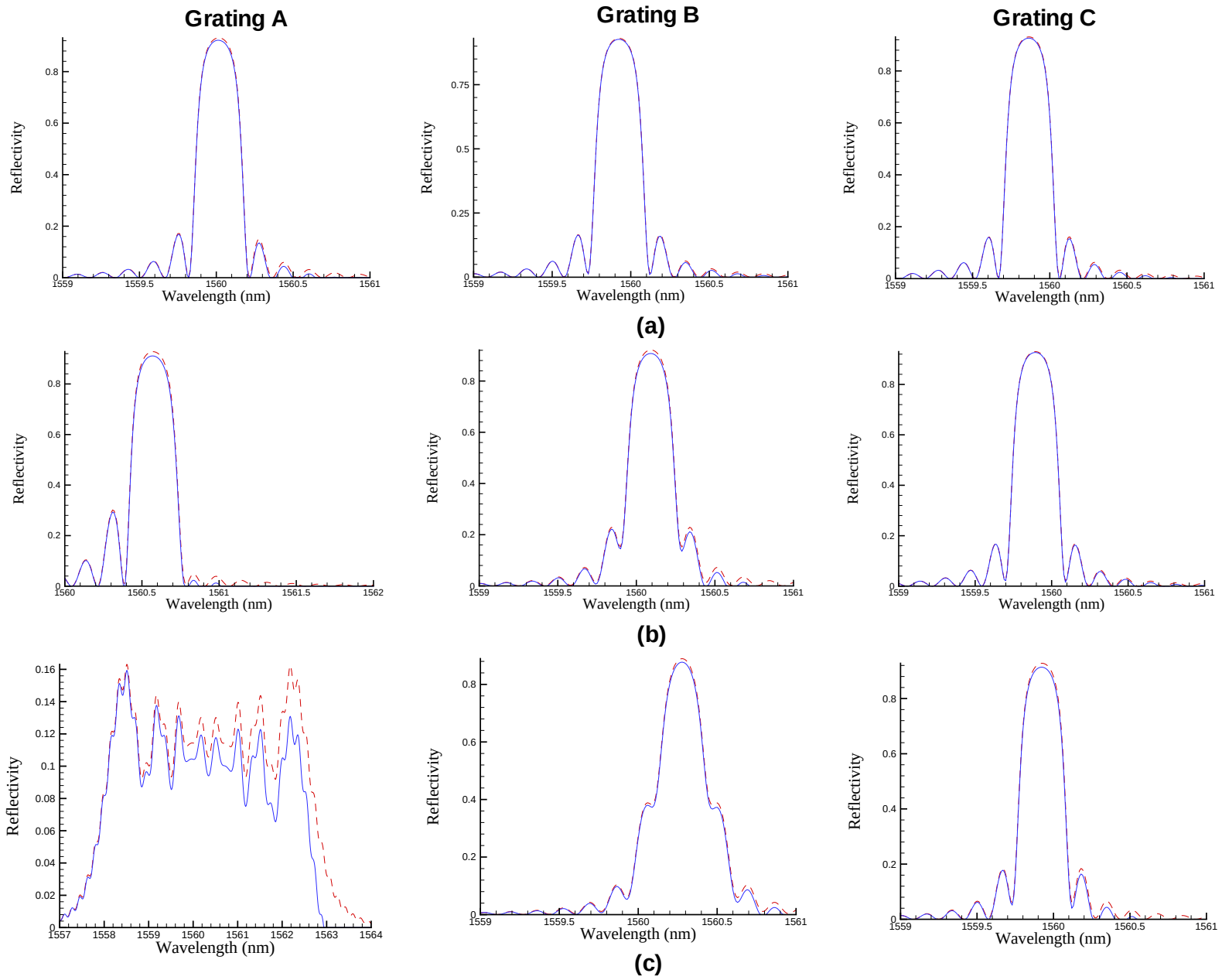

Figure 5.12: Reflected spectra of gratings A, B, and C for different crack lengths: (a) layers 1-3 broken; (b) layers 1-5 broken; (c) layers 1-7 broken. Simulated spectrum including only axial strain is plotted as a dashed line. Simulated spectrum including both axial strain and bending loss is plotted as a solid line.

be σ_0, obtained from the FEA results i.e.

$$\sum_{j=1}^{n-1}(a_j + b_j)\frac{\psi_{j,8}}{t_8} = \sigma_0 - \frac{E^{(8)}}{E_f} \tag{5.5}$$

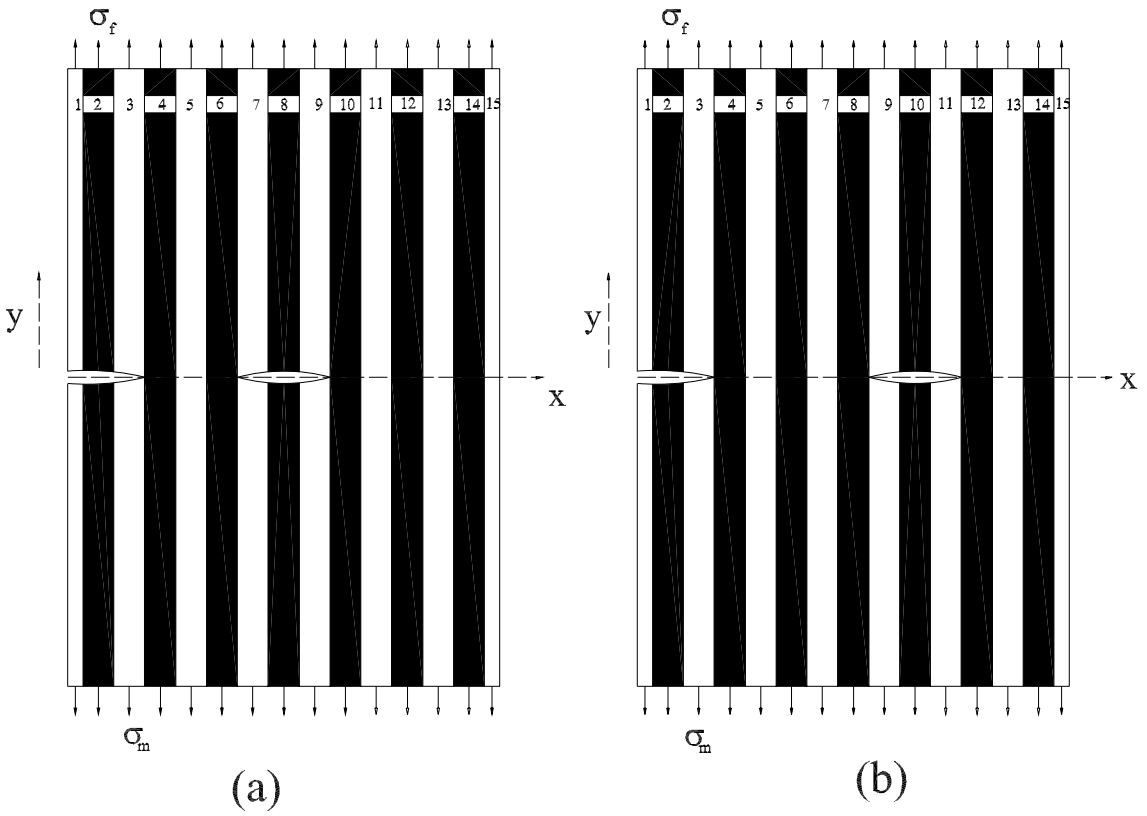

Figure 5.13: Geometry of unidirectional composite defining multiple crack locations (note, only one-half of composite is shown, due to symmetry about y-axis). (a) Cracks located at a distance of two fibers from one another. (b) Cracks located at a distance of three fibers from one another.

Figure 5.14 plots the average axial stress obtained using both the optimal shear-lag theory and FEA for the crack geometry of Fig. 5.13(a), incorporating the above boundary conditions into the shear-lag theory. Fig. 5.15 shows the comparison between FEA and the shear-lag model of the average axial stress for the crack geometry of Fig. 5.13(b).

Although the optimal shear-lag theory is an efficient method for obtaining the form of the average axial stresses in each layer for a center crack in a unidirectional composite, it requires extra knowledge such as the stress concentration at the crack tip in order to model multiple cracks along a single crack plane. When the cracks are situated on different or the

same y-plane, far from the boundaries and from each other, the shear-lag theory can be applied. If the cracks are on different planes and close to one another then shear-lag theory does not produce satisfactory resutls. In general, if one wants to model a composite with all possible crack configurations, then one has to adopt another numerical method to estimate stresses far from the location of the crack.

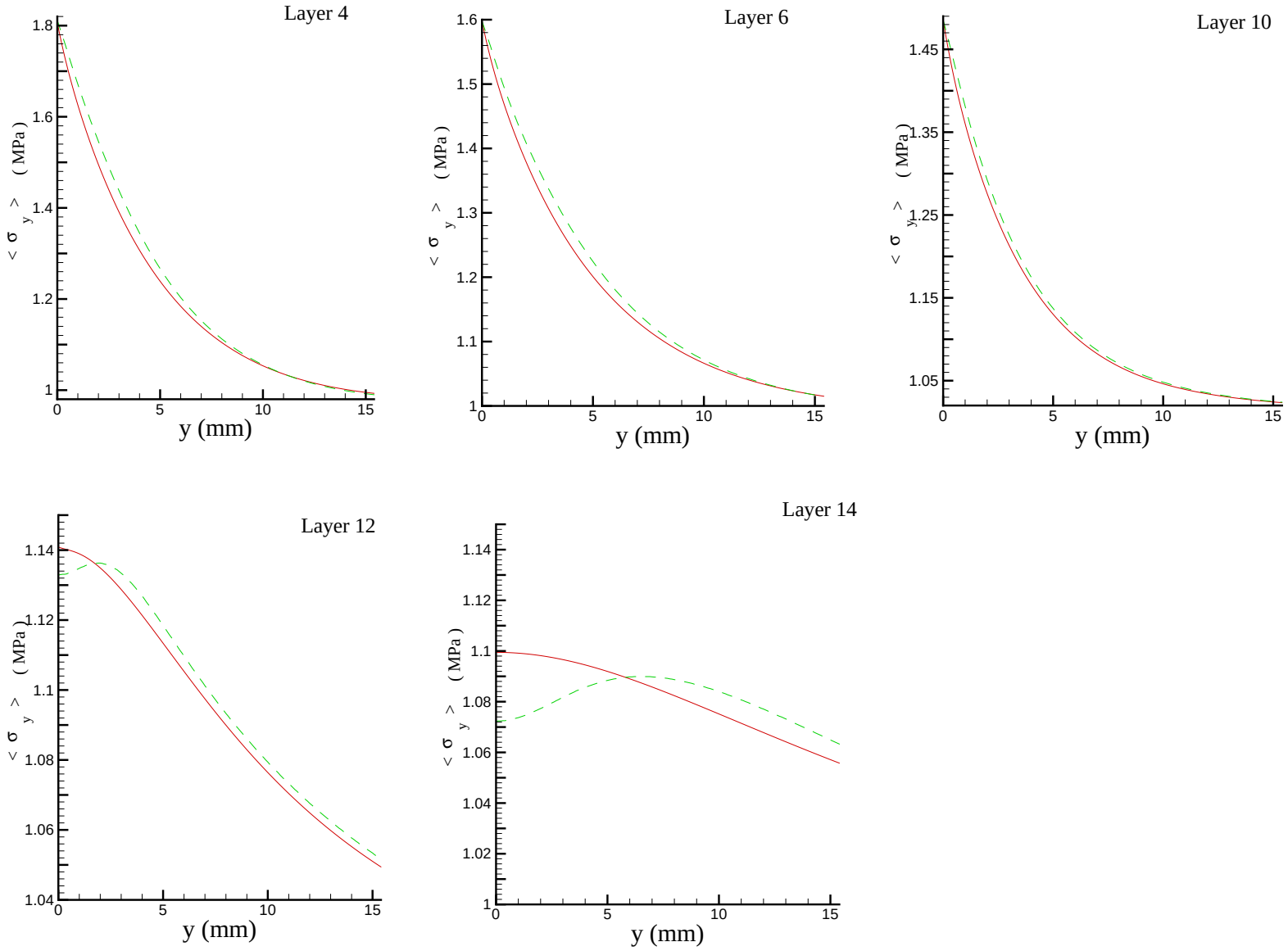

Figure 5.14: Average axial stress $< \sigma_y >$ in the fiber layers $4, 6, 10, 12$ and 14 for the crack geometry of Fig. 5.13(a).

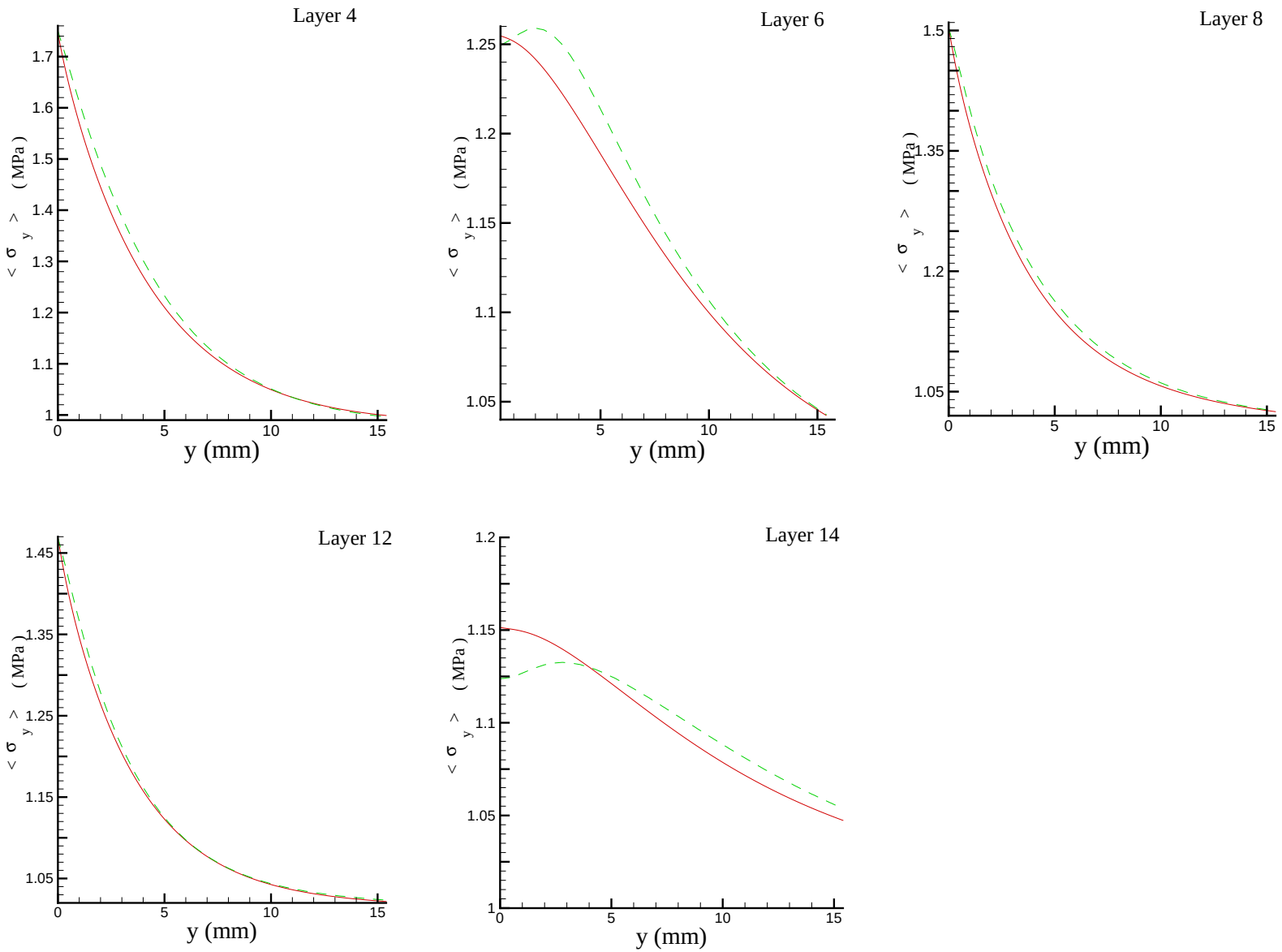

Figure 5.15: Average axial stress $< \sigma_y >$ in the fiber layers $4, 6, 8, 12$ and 14 for the crack geometry of Fig. 5.13(b).

Chapter 6

Conclusions

The goal of this thesis is to measure and simulate the response of the optical fiber Bragg grating sensor to multi-component loading for future integration into the structural health monitoring of composites. This thesis presents a simulation method to determine the effects of fiber bending and shear loading on an embedded optical fiber Bragg grating sensor. The effect of shear loading is shown to be negligible even when the fiber coating is not included.

The use of an optical fiber Bragg grating sensor to measure non-uniform axial strain was demonstrated by embedding the grating in a conical specimen, cantilevered at the base and subjected to a point load at the apex. The dependence of bending loss on the radius of curvature was experimentally measured. The analytically simulated grating response, including the effects of bending, for varying non-uniform applied axial strains correlated well with the experimental response. The exact cone solution also correlated well with the average axial strain measured in the grating, however not the distribution of strain. In order to obtain a better comparison with the exact strain distribution, a numerical model of the specimen and exact loading and support conditions would be required.

A numerically efficient optimal shear-lag theory was applied to calculate the sensor response when the Bragg grating is embedded in a fiber reinforced composite. The limits of the shear-lag theory were shown through comparison with a finite element analysis for both single crack and multiple crack cases. The response of sensors embedded in a single fiber layer at different locations was simulated for different transverse crack lengths including

the bending effects. This work demonstrates the use of a numerically efficient method to calculate the sensor response using both FEA and optimal shear-lag theory including the effects of multicomponent loading. The shear-lag theory calculates the response of the sensor when there is no damage present near the sensor. When damage is indicated, the FE model is used, including the effects of bending loss on the response of the sensor.

This work is a first step towards the development of embedded sensors for fiber-reinforced composites that are "self evaluating". Fiber optic sensor reliability in the long term still remains an open question, particularly due to large-scale manufacturing difficulties or in applications pertaining to severe environments and loading conditions, such as impact induced structural damage. There are several failure modes of the sensors themselves which could then be incorrectly processed as failures of the host material, including microbending along the optical fiber, fiber breakage, and degradation of the optical fiber due to chemical reactions or moisture. The separation of these effects from those in the surrounding material requires more sensor information detail, such as that presented in this work, rather than simply the average strain along the sensor.

Bibliography

[1] C. Boller, "Ways and options for aircraft structural health management", *Smart Materials and Structures*, Vol. 10, pp. 432–440, 2001.

[2] R. M. Jones, "Mechanics of composite materials", *Taylor and Francis*, 1999.

[3] R. M. Measures, "Structural monitoring with fiber optic technology", *Academic Press*, 2001.

[4] E. Udd, "An overview of fiber-optic sensors", *American Institute of Physics*, Vol. 66, pp. 4015–4030, 1995.

[5] R. Kashyap, "Fiber Bragg gratings", *Academic Press*, 1999.

[6] R. J. Van Steenkiste, L. P. Kollàr, "Calculation of the stresses and strains in embedded fiber optic sensors", *Journal of Composite Materials*, Vol. 32, pp. 1647–1679, 1998.

[7] R. M. Measures, "Smart composite structures with embedded sensors", *Composites Engineering*, Vol. 2, pp. 597–618, 1992.

[8] C. M. Lawrence, D. V. Nelson, T. E. Bennett, J. R. Spingarn, "An embedded fiber optic sensor method for determining residual stresses in fiber-reinforced composite materials", *Journal of Intelligent Material Systems and Structures*, Vol. 9, pp. 788–799, 1998.

[9] C. Dai, D. Yang, X. Tao, H. Tam, "Effects of pure bending on the sensing characteristics of fiber Bragg gratings", *Proceedings of SPIE*, Vol. 4077, pp. 92–96, 2000.

[10] X. Dong, H. Meng, Z. Liu, G. Kai, X. Dong, "Bend measurement with chirp of fiber Bragg grating", *Smart Materials and Structures*, Vol. 10, pp. 1111–1113, 2001.

[11] K. Peters, P. Pattis, J. Botsis, P. Giaccari, "Experimental verification of response of embedded optical fiber Bragg grating sensors in non-homogeneous strain fields", *Optics and Lasers in Engineering*, Vol. 33, pp. 107–119, 2000.

[12] K. Peters, M. Studer, J. Botsis, A. Locco, H. Limberger, R. Salathe, "Embedded optical fiber Bragg grating sensors in a nonuniform strain field: measurements and simulations", *Experimental Mechanics*, Vol. 41, pp. 19–28, 2001.

[13] J. A. Nairn, D. A. Mendels, "On the use of planar shear-lag methods for stress-transfer analysis of multilayered composites", *Mechanics of Materials*, Vol. 33, pp. 335–362, 2001.

[14] Z. Xia, T. Okabe, W. A. Curtin, "Shear-lag versus finite element models for stress transfer in fiber-reinforced composites", *Composites Science and Technology*, Vol. 62, pp. 1141–1149, 2002.

[15] T. Erdogan, "Fiber grating spectra", *Journal of Lightwave Technology*, Vol. 15, pp. 1277–1294, 1977.

[16] H. F. Taylor, "Bending effects in optical fibers", *Journal of Lightwave Technology*, Vol. LT-2, pp. 617–628, 1984.

[17] R. J. Van Steenkiste and L. P. Kollàr, "Effect of the coating on the stresses and strains in an embedded fiber optic sensor", *Journal of Composite Materials*, Vol. 32, pp. 1680–1711, 1998.

[18] C. F. Gerald and P. O. Wheatley, "Applied numerical analysis", *Addison-Wesley*, pp. 448-524, 1999.

[19] J. D. Renton, "Pure bending of a solid cone", *Journal of the Mechanics and Physics of Solids*, Vol. 45, pp. 753–761, 1997.

[20] J. D. Renton, "The characteristic response of hollow cones", *Journal of Elasticity*, Vol. 49, pp. 101–112, 1998.

Appendix A

Drawings of Loading frame and Mold for Conical Specimen

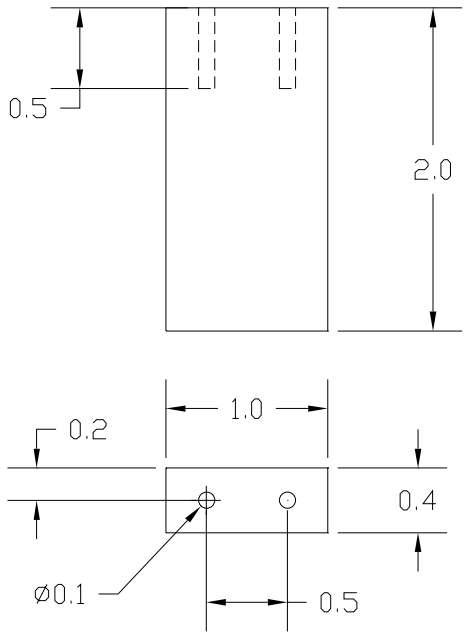

Figure A.1: Adaptor piece for the grip of the Instron machine (dimensions in inches).

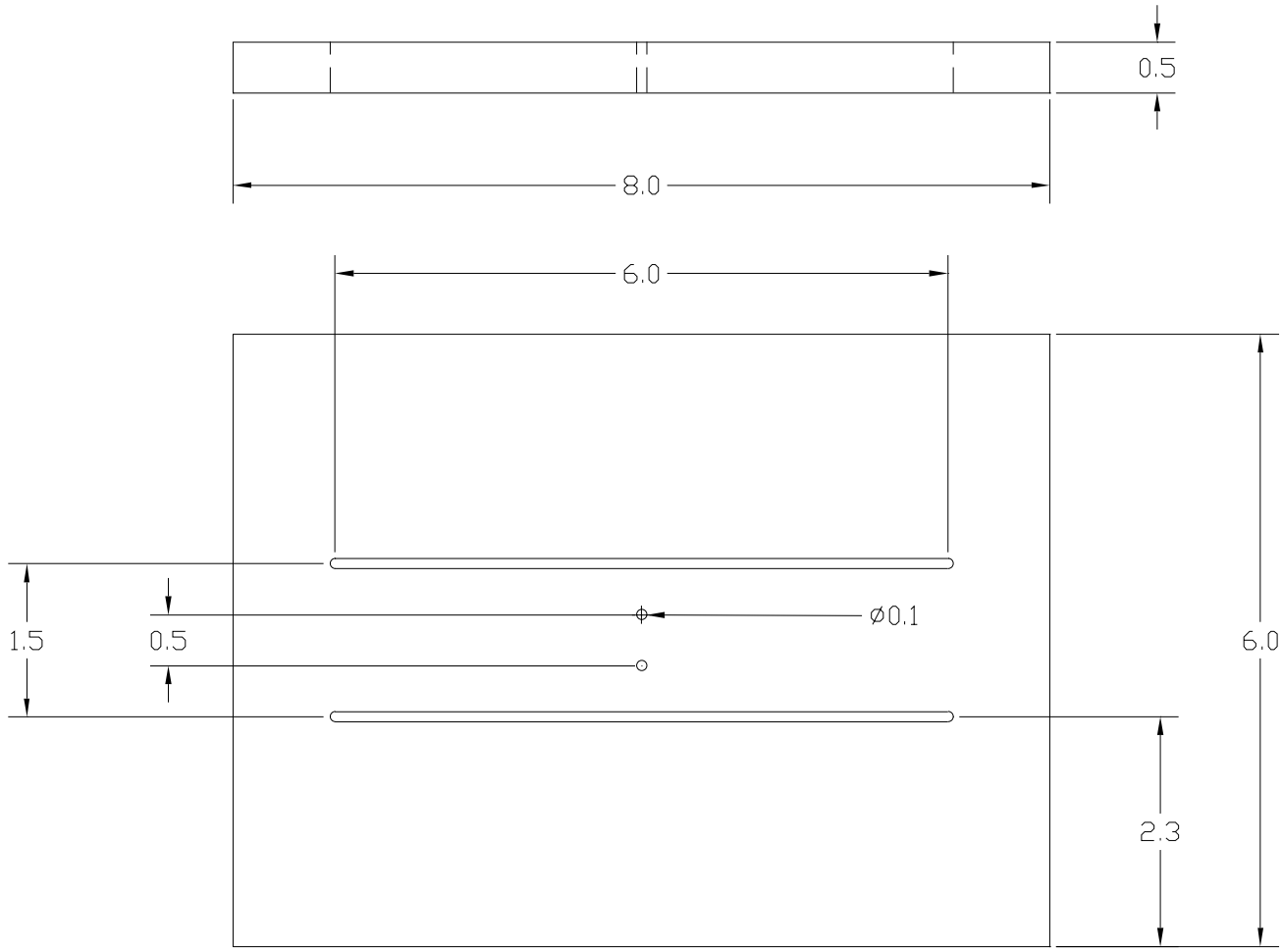

Figure A.2: Base plate (dimensions in inches).

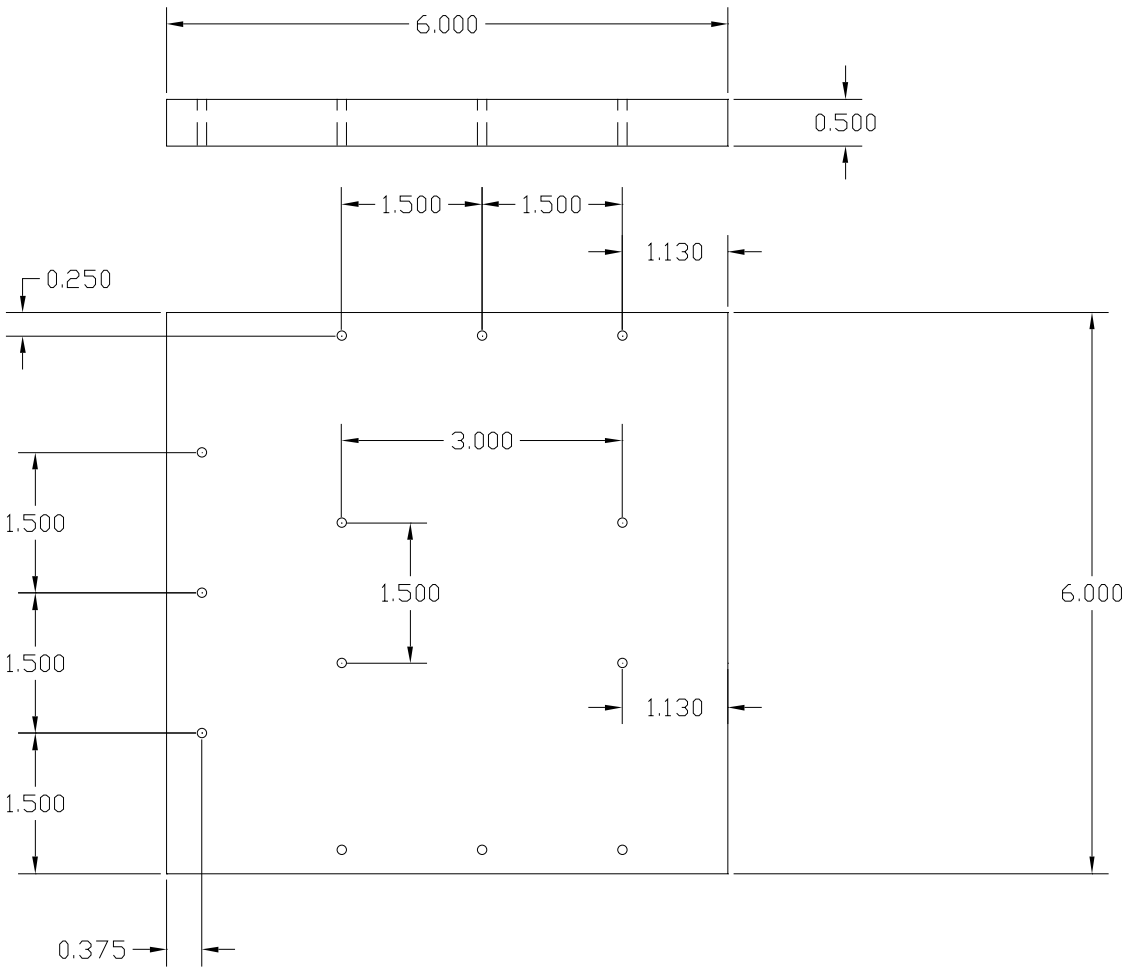

Figure A.3: Sliding horizontal plate of the L-frame (dimensions in inches).

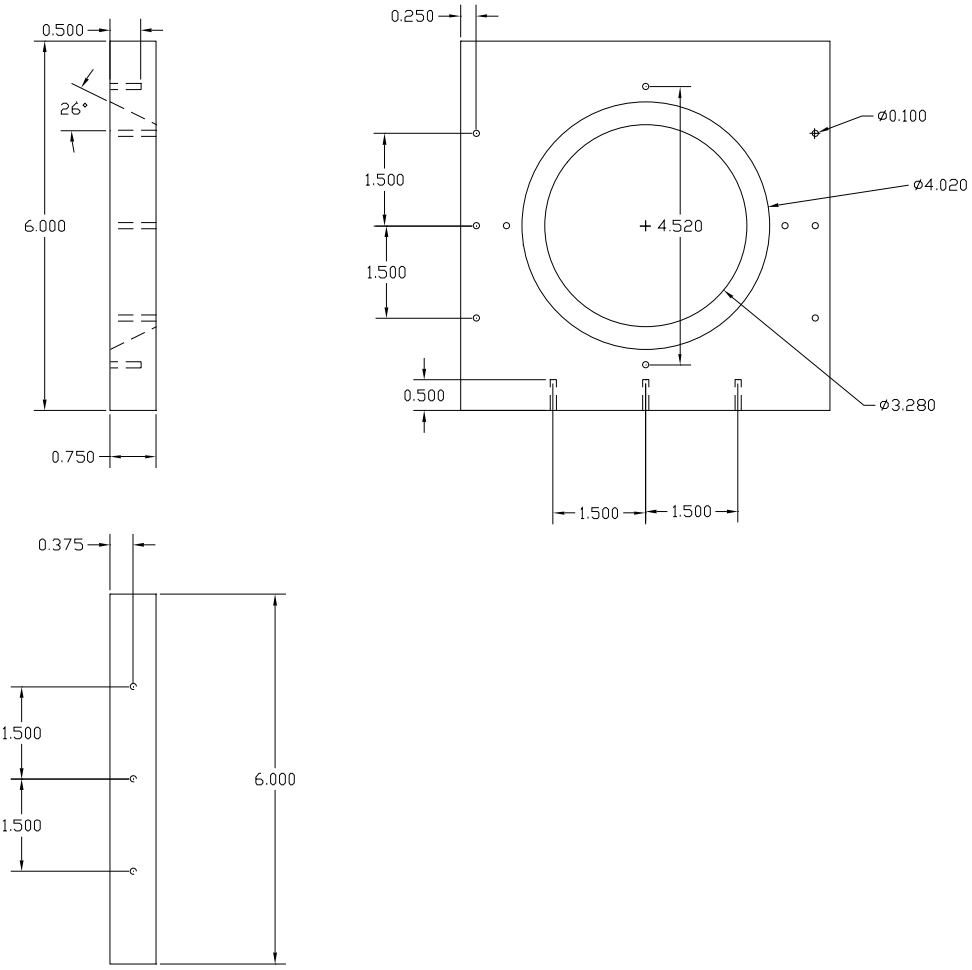

Figure A.4: Vertical plate of the L-frame to which the specimen base is mounted (dimensions in inches).

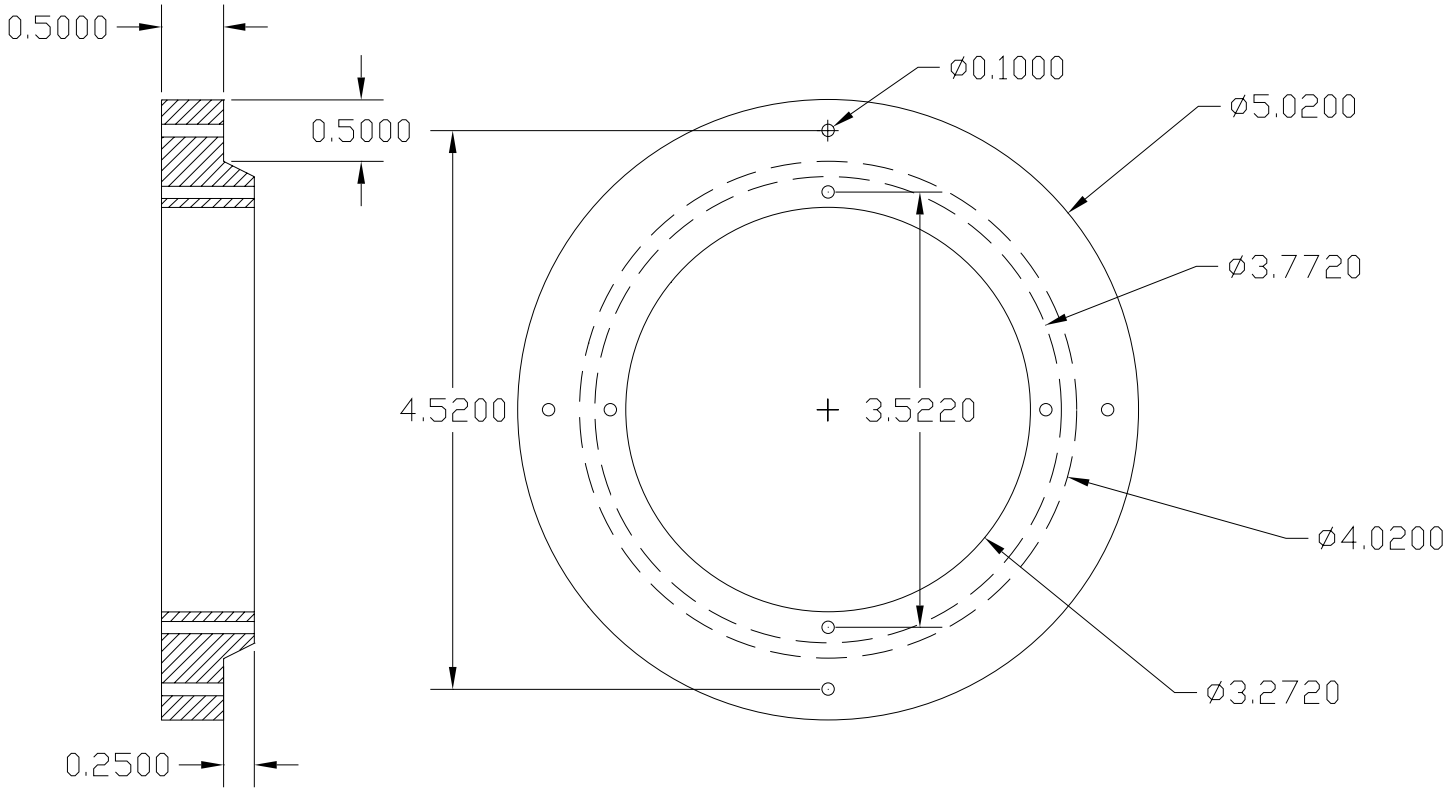

Figure A.5: Collar to grip the specimen firmly (dimensions in inches).

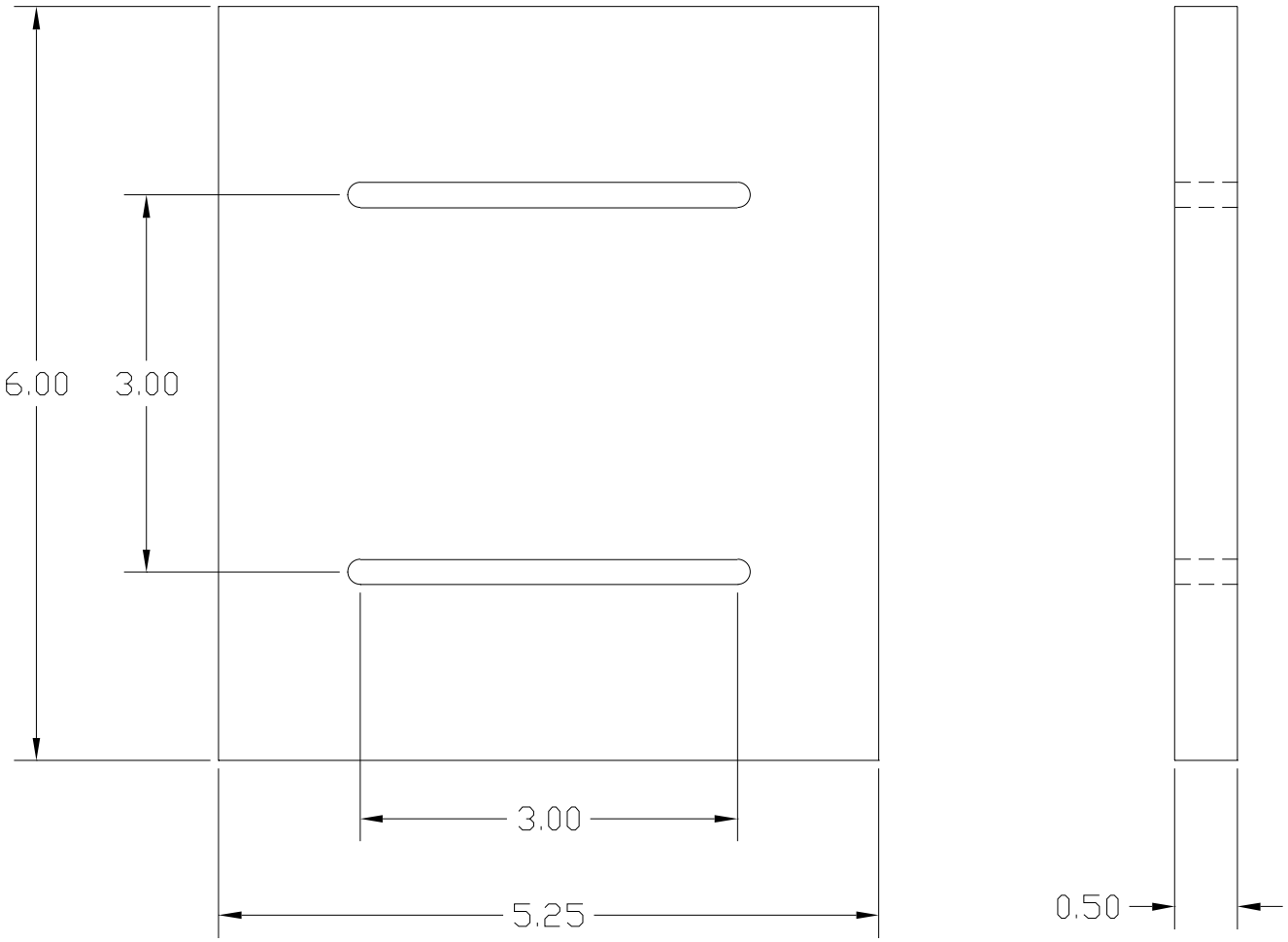

Figure A.6: Gusset that prevents the L-frame from deforming. Also included are slots in which guides slide (dimensions in inches).

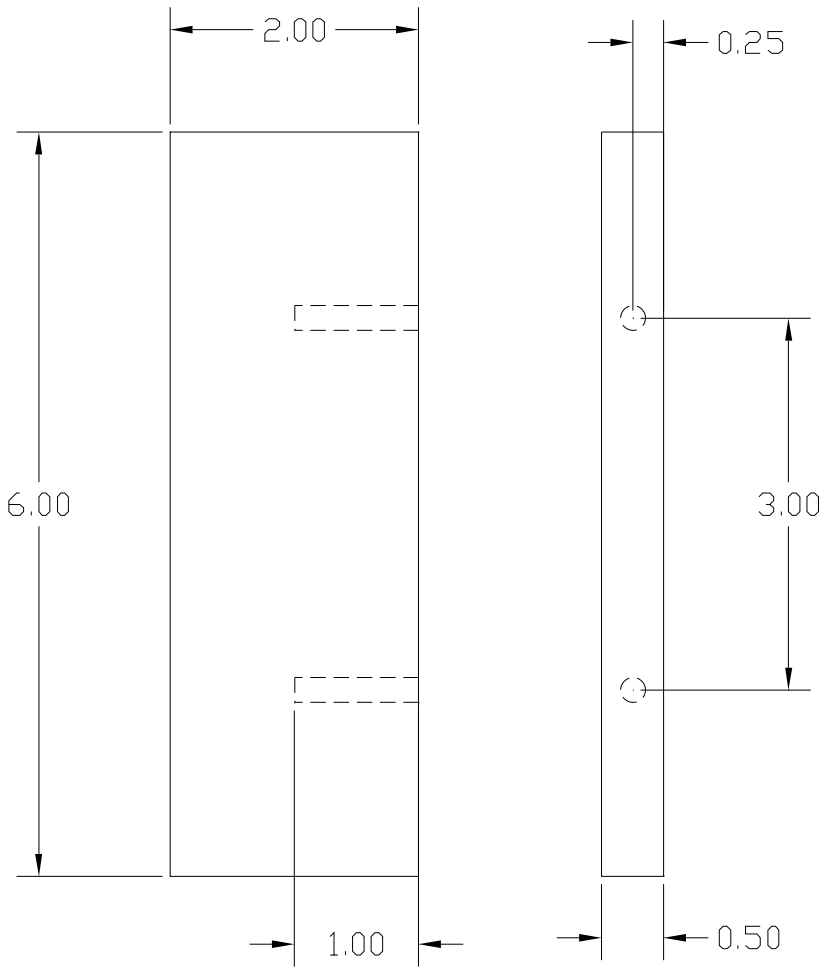

Figure A.7: Guides for loading bar (dimensions in inches).

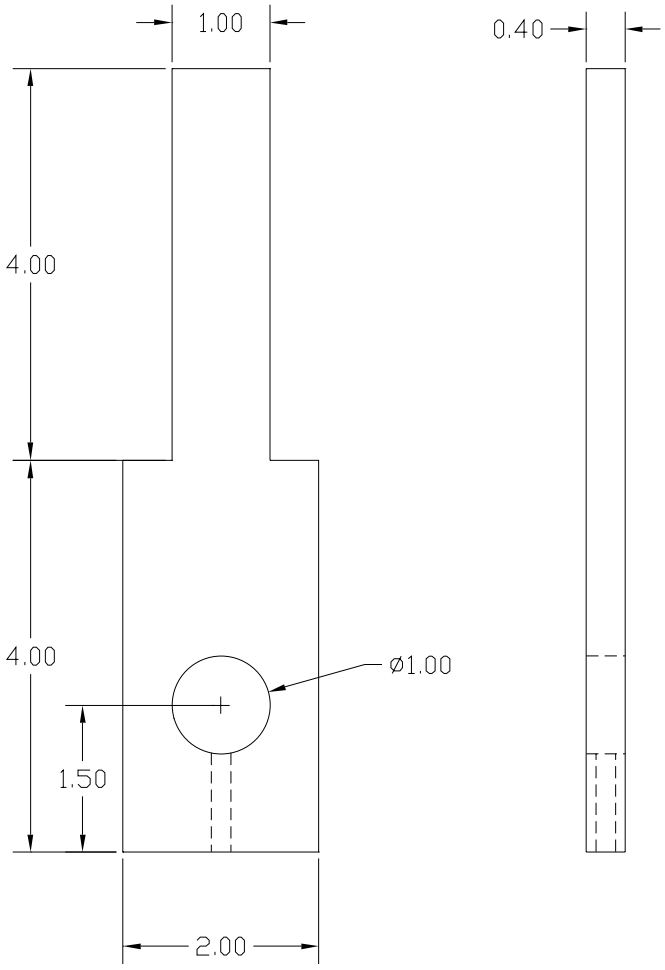

Figure A.8: The loading bar. The screw at the bottom ensures an applied point load (dimensions in inches).

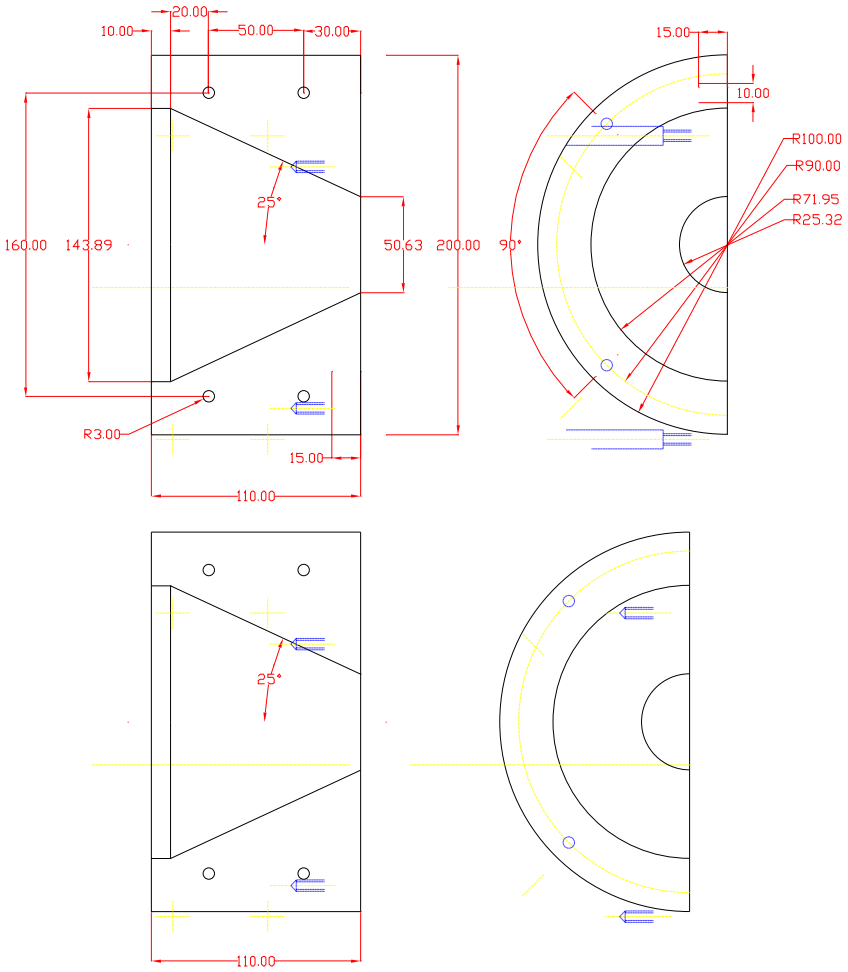

Figure A.9: The first half of the mold in two parts (dimensions in mm). When machining both the halves were machined as one single half.

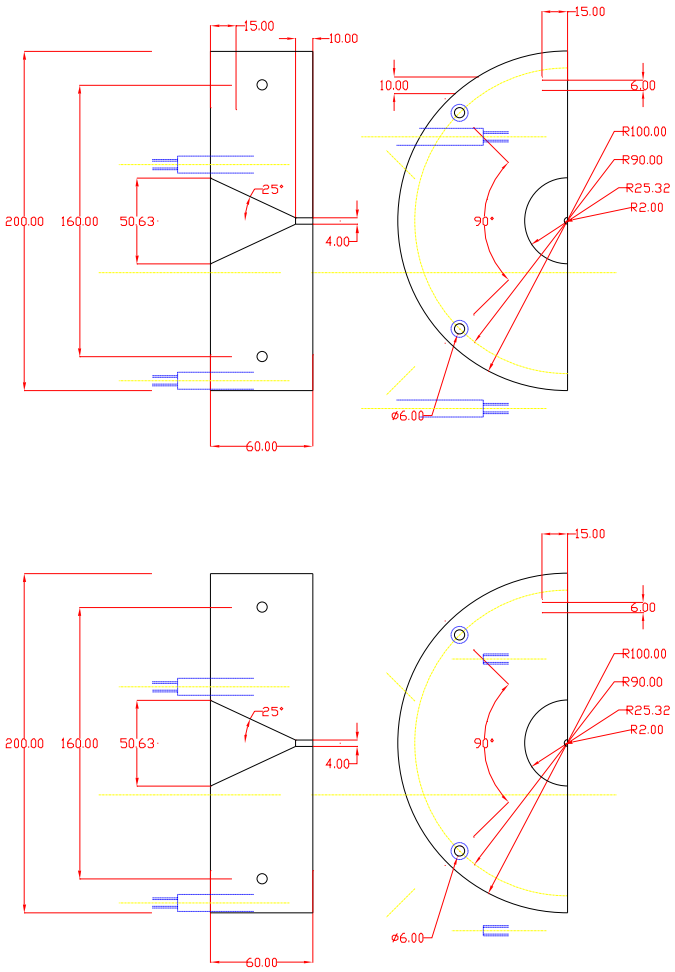

Figure A.10: The second half of the mold in two parts (dimensions in mm).